INTERNATIONAL JOURNAL OF
**ENERGY RESEARCH** WILEY

# Design of power-blocks for medium-scale supercritical carbon dioxide plants

Ambra Giovannelli[1]  |  Erika M. Archilei[1]  |  Giuseppina Di Lorenzo[1]  |
Coriolano Salvini[1]  |  Muhammad A. Bashir[1,2]  |  Giuseppe Messina[3]

[1]Department of Engineering, Roma Tre University, Rome, Italy

[2]Department of Mechanical Engineering, Mirpur University of Science and Technology (MUST), Mirpur, Pakistan

[3]Energy Technology Department, ENEA Casaccia Research Center, Rome, Italy

**Correspondence**
Ambra Giovannelli, Department of Engineering, Roma Tre University, Via della Vasca Navale 79, Rome 00146, Italy.
Email: ambra.giovannelli@uniroma3.it

**Summary**

For power production, the emerging technologies of supercritical carbon dioxide (S-$CO_2$) cycles show potential advantages if compared to conventional plants. The current bottleneck in exploiting such cycles is the development of novel components such as turbomachines and heat-exchangers. This paper focuses on the layout arrangement and machinery design of a novel power-block for a 10 to 15 MW supercritical carbon dioxide plant. The applied design procedure involves 0D and 1D models implemented using an in-house Fortran code, and 3D computational fluid dynamics (CFD) analyses using ANSYS-CFX. Novel configurations of the power block were designed, starting with the same primary thermal source. At nominal conditions, expected overall output powers from 13.2 to 16.2 MW were found. Finally, some qualitative considerations were included in the discussion to compare the analysed arrangements.

**KEYWORDS**

centrifugal compressor, CFD, radial turbomachinery design, radial-inflow turbine, recompressed Brayton cycle, supercritical $CO_2$

## 1 | INTRODUCTION

It is widely accepted that climate change is one of the largest environmental issues of the twenty-first century. One of the key challenges it presents is how to achieve a massive reduction in greenhouse gas emissions – which are considered to be one of the main contributors to climate change – while also meeting the world's growing energy needs, both without affecting the sustainability, affordability, and reliability of any service.[1] To do so, it will be essential to reduce greenhouse gas emissions, not only in the power generation sector, which has so far taken centre stage in any decarbonization plans put forward, but also across several other sectors.[2] Different strategies, such as increasing the efficiency of energy conversion systems, moving toward widespread use of renewable energy sources, and implementing carbon capture and storage (CCS) technologies are being explored in this context.

An emerging technology, based on energy conversion cycles using Supercritical $CO_2$ (S-$CO_2$) as working fluid, can play a positive role in the strategies mentioned above and be exploited in different sectors. S-$CO_2$ cycles use carbon dioxide as a working fluid with a compression process near the critical point of $CO_2$.[3] Motivated by the

---

**Abbreviations:** EXP, expander; GEN, electrical generator; HPE, high-pressure expander; HTR, high-temperature recuperator; LTR, low-temperature recuperator; MC, main Compressor; MOT, electrical Motor; RAMS, reliability, availability, maintainability and safety; RC, recompression compressor; RCBC, recompression Brayton cycle; SST, shear stress transport; WF, working fluid; WHRU, waste heat recovery unit.

need to increase the thermodynamic efficiency of Brayton-Joule power cycles, the idea of using S-$CO_2$ as working fluid dates back to the 1960s and the work by Angelino[4,5] and Feher.[6,7] As a result of the real gas effects and low compressibility of $CO_2$ near the critical point, the compression work in the S-$CO_2$ cycle is relatively lower and the cycle efficiency relatively higher when compared to other conventional cycles. In addition to the high efficiency, other favourable features that characterize this technology, and which open several potential markets for its application, include[8,9]: near-zero emissions, cost reduction, compactness, high load-flexibility and possible integration with renewable energy sources.

These advantages have led to an increased interest in the applicability of the S-$CO_2$ technology in the waste-heat-recovery field, where it is an appealing alternative to the ORC option.[10] In this case, the S-$CO_2$ technology can be coupled with a variety of heat sources. Primarily proposed in conjunction with nuclear power reactors[11] and for the concentrated solar power generation,[12,13] it has also shown promise for use with combined cycle power plants,[14,15] with fuel cells[16,17] and geothermal power.[18] In addition, this application of the S-$CO_2$ technology has potential value in the marine propulsion sector.[19]

In a S-$CO_2$ cycle the working fluid is compressed (or pumped) up to the maximum pressure and heated to the maximum temperature in a heat exchanger (Waste Heat Recovery Unit). It is then expanded in a turbine, and finally cooled down to close the cycle. Several modifications of the S-$CO_2$ cycle to enhance the technical feasibility and the economic attractiveness of the technology have been proposed and investigated.[8] One such proposal is the use of a recuperator, through which a considerable portion of the heat available at the turbine exit is recovered to pre-heat the compressed fluid before it enters the waste recovery unit, thus improving cycle efficiency. However, due to the nonlinear change of physical properties of $CO_2$ near the critical point, this approach may produce some particular phenomena in the recuperator, such as the internal pinch point. This has a negative impact on the effectiveness of the heat exchanger and, in turn, on the whole cycle performance. Another promising modification is the so-called Re-Compression Brayton Cycle (RCBC) configuration. As the name suggests, there is a Re-Compressor (RC) in addition to the Main Compressor (MC) in this S-$CO_2$ cycle configuration, which means the stream is divided into two parts for the compression phase. In addition, the recuperator is replaced by two separate heat exchangers: the High Temperature Recuperator (HTR) and Low Temperature Recuperator (LTH). After being compressed in the main compressor, the first stream flows into the low temperature recuperator; the second stream is first compressed in the

re-compressor, and then injected into the first stream at the outlet of the low temperature recuperator. The change in mass flow rate alleviates the internal pinch-point issue, as it ensures more balanced heat capacities on the hot and cold sides of the recuperator. A concept plant scheme of the RCBC in shown in Figure 1.

The supercritical recompression configuration has received considerable attention in the literature, not only for its ability to mitigate the internal pinch-point issue, but also for several additional strengths.[8] In particular, the design of turbomachines has been widely investigated, as it is crucial to advancing any R&D efforts related to this technology. Several studies have focused on this topic; however, all concern large-scale (100 MW and over) and small scale (up to 1 MW) cases (eg,[20,21]), whereas the medium-size cases have received limited attention.

When designing a new S-$CO_2$ power group unit, it is of paramount importance to choose the most suitable layout for the turbomachines. Several factors come into play, including component specifications and related fluid dynamic and mechanical constraints. Another key aspect that needs to be addressed is the operational flexibility of the unit, including fast start-ups and shutdowns. Several configurations have been proposed, based on both the aforementioned aspects and the size of the reference plant. Fleming et al[22] give a preliminary classification of possible options for the selection of machinery layouts and major components based on plant size. They consider the following aspects: single or multiple shaft layouts; turbines and compressors type (radial/axial machines, number of stages, shrouded/un-shrouded); bearings (gas foil, magnetic, hydrostatic, hydrodynamic
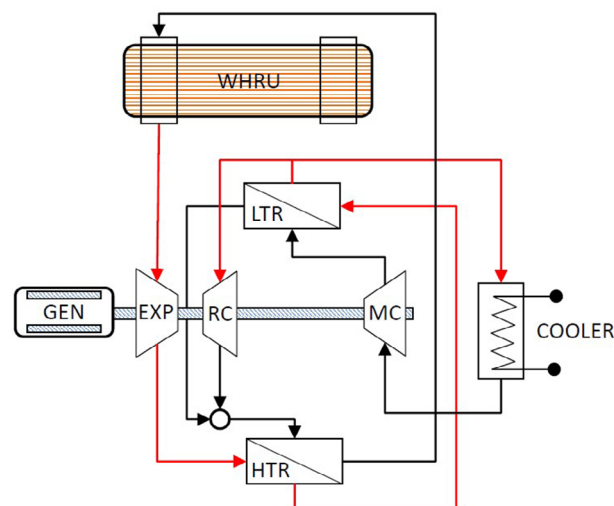


**FIGURE 1**    Reference plant scheme [Colour figure can be viewed at wileyonlinelibrary.com]

oil); seal technology; control of windage losses; and electric motor/generator type (permanent magnet, geared options, synchronous generators). While limited options were reported for both small (up to 1-5 MWe) and large (over 50 MWe) scale power blocks, it was noted that several alternatives in terms of shaft configuration (single/multiple), turbomachinery components (radial/axial), bearings (magnetic/hydrodynamic) and electric machines (gearbox/synchronous) exist for medium (10-15 MWe) systems. However, only a handful of studies have examined closely this variety of options in the design process of a medium-scale unit.

Kalra et al[23] consider how a 5 to 10 MWe power block might be best designed for a RCBC to be installed in a Concentrated Solar Power (CSP) plant. The following four feasible layouts were selected based on fluid dynamic and mechanical considerations, as well as technology maturity (mainly for compressors, bearings, seals and electric machines):

1. A direct drive or geared turbo-generator. In such a configuration both the MC and RC are driven by electric motors.
2. A geared layout, with the compressor train on one shaft and the expander on another shaft at a different speed. Both are connected to the shaft of the electric machine.
3. A dual-shaft configuration, in which both compressors are moved by the High-Pressure Expander (HPE) on a high-speed shaft and a power turbine directly connected to the electric generator. The HPE is aerodynamically connected with a power turbine.
4. All the turbomachines on a high-speed shaft with a geared generator.

The authors do not identify a "best option" from a techno-economic standpoint, as a down-selection activity required technical information not yet available. However, they offer several insightful considerations (ie, advantages and drawbacks of each configuration) and provided a preliminary design of the power turbine.

A more detailed conceptual design for a 10-MWe scale power system is presented by McDowell et al.[24] In this case, a dual-shaft configuration (as identified in above list) was selected to favour turbomachinery and whole cycle efficiency. This system consists of two one-stage centrifugal compressors (both MC and RC), coupled with a four-stage axial turbine on a high-speed shaft (39 000 rpm) and a power turbine spinning at lower speed (25 000 rpm). A more comprehensive component design for a 10-MWe system was reported by Heshmat et al,[25] who considered several mechanical issues related to rotodynamic aspects and selection of bearings,[26] as

well as the availability of suitable high-speed electric generators. In this study, the following layouts were outlined, beginning with a single-shaft layout with a geared connection to the generator:

- A mechanically coupled power train with a split gearbox connected to two twin 5 MWe alternators.
- An electrically coupled power train made of two separated shafts. One shaft is for MC and RC compressors and is driven by an induction motor, while the other shaft is for the turbine and connected by a gearbox to a generator.
- An electrically coupled power train made of three different shafts. The layout is similar to the previous, but the compressors are mounted on different shafts and moved independently by two electric motors.
- A dual-shaft configuration similar to the system presented above,[23] but instead with the high-pressure turbine connected to the electric generator and compressors connected to the low-pressure turbine.
- A three-shaft variation of the previous layout, in which MC and RC are decoupled and moved independently by two twin low-pressure turbines.

The study does not identify a best configuration, but instead considers all to be suitable based on the technological readiness of mechanical and electric components.

From a thermodynamic perspective, more information (although partial) is available in[27] where the authors give a preliminary design of a three-shaft layout for a 10-MW power-block and in the literature, throughout which design cases, CFD analyses and preliminary tests on small prototypes are reported for $CO_2$ centrifugal compressors. This literature was considered in the preliminary design phase of the turbomachines (detailed in Section 3), despite the fact that it refers to units smaller than those analysed in this paper.

This work adds to the existing literature by presenting a comprehensive design exercise for both turbomachines of a medium-size unit (15 MW). In addition, the study integrates zero-dimensional (0D), one-dimensional (1D) and three-dimensional (3D) models, provides an improved prediction of the turbomachine performance, and investigates several layouts to determine the optimal one. The key novelty of this work is its detailed design of three three-shaft layouts, not found in the previous literature, which show interesting features for a medium-size power plant. They were analysed and compared quantitatively (in terms of expected performance at nominal conditions) and qualitatively (eg, machinery flexibility at part load).

The paper is composed of five sections including this introduction. Section 2 describes the reference power

plant and potential power-block layouts. Section 3 focuses on methodological approaches adopted for the preliminary and detailed designs of each component. Design results are shown in Section 4, which is organized in several sub-sections – one for each main components of the power system: main compressor, recompressor and expanders. Since the designs of the main compressor and the expanders depend on the power-block layout, these sub-sections are sub-divided into two parts based on the reference configuration. A summary of the main results, concluding remarks and suggestions for further research activities are given in the final section.

## 2 | 15 MWE POWER SYSTEM DESCRIPTION

The reference RCBC was designed and optimized from the thermodynamic point of view for a medium-scale (10-15 MWe) waste heat recovery unit. This work is a result of ongoing R&D activities at the Italian National Agency for New Technologies, Energy and Sustainable Economic Development aimed at studying and optimizing novel S-CO$_2$ cycles.[28] Still in the conceptual phase, at design conditions this RCBC operates between 75 to 300 bar and 35°C to 650°C. Accordingly, the CO$_2$ should always remain supercritical. The cycle was optimized by maximizing the overall cycle thermal efficiency (ie, by maximizing internal heat recoveries with a high- and a low-temperature recuperator). Main boundary conditions for the power system (eg, nominal pressures, temperatures and mass flow rates) were derived from the cycle optimization and, subsequently, inputted into the machinery design process. Such data are reported in Table 1.

The unconventional nature of the working fluid, as well as significantly different thermodynamic conditions relative to conventional power cycles, lead to a design problem, which is intrinsically fraught with uncertainties. Three layouts, outlined below and shown in Figure 2, were considered for the preliminary design of a power group for the 10 to 15 MWe S-CO$_2$ power plant described above:

- A dual-shaft scheme inspired by the one proposed by Kalra.[23] The MC and RC are mounted on the high-speed shaft and moved by the HPE, while the power turbine is connected to the electrical generator (Figure 2A).
- A three-shaft scheme, in which the MC is a two-stage centrifugal compressor. The first MC stage is moved at a lower speed by an independent electric motor to avoid liquid in the machine in on-design and

**TABLE 1** Key data as resulting from RCBC optimization[27]

| Parameter | Unit | Value |
|---|---|---|
| Main compressor | | |
|     Mass flow rate | (kg/s) | 150 |
|     Inlet temperature | (°C) | 35 |
|     Inlet pressure | (bar) | 75.3 |
|     Outlet pressure | (bar) | 233.4 |
| Recompressor | | |
|     Mass flow rate | (kg/s) | 50 |
|     Inlet temperature | (°C) | 129 |
|     Inlet pressure | (bar) | 76.8 |
|     Outlet pressure | (bar) | 233.4 |
| Turbine | | |
|     Mass flow rate | (kg/s) | 200 |
|     Inlet temperature | (°C) | 650 |
|     Inlet pressure | (bar) | 233 |
|     Outlet pressure | (bar) | 78.1 |

off-design conditions. The MC second stage, the RC and the HPE remain coupled together on the high-speed shaft. The power turbine is connected to the generator (Figure 2B).
- A three-shaft scheme where the multi-stage centrifugal MC is moved by a dedicated electric motor to improve the machinery flexibility, while the RC is coupled with the HRE on the high-speed shaft. The power turbine is on another shaft at a lower-speed and is connected to the generator (Figure 2C). A variant of this layout, in which the multi-stage MC is connected to the power turbine instead of being installed on a separated shaft, is reported in Figure 2D.

The design procedure was followed starting with the simplest concept. The system layout was modified according to fluid-dynamic and thermodynamic results.

## 3 | DESIGN METHODOLOGY

The preliminary design for the power-block components was developed using the procedure described in.[29] After determining possible system layouts, both the rotational speed and the preliminary configuration of all components (eg, radial/axial machines, number of stages for each component) were selected according to similarity rules. However, this selection was not definitive. Options were narrowed down based on constraints related to the technical readiness of specific components (eg, electric generators and motors, seals and bearings), the
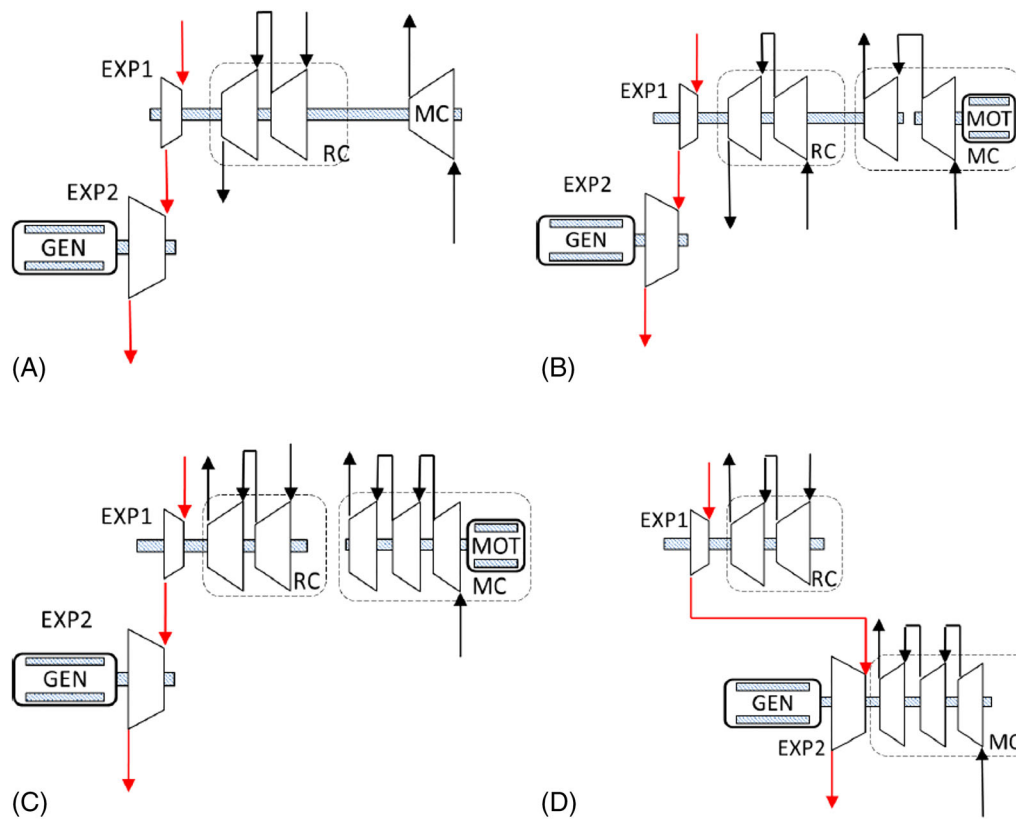
**FIGURE 2**    Power system layouts [Colour figure can be viewed at wileyonlinelibrary.com]

availability of materials, and/or reliability, availability, maintainability and safety (RAMS) considerations. These options first informed the 1D preliminary design and, later, the detailed three-dimensional thermodynamic and aerodynamic design. For unconventional working fluids like S-$CO_2$, the design process can be highly iterative: 1D and 2D models, based on semi-empirical correlations, can differ significantly from 3D numerical or experimental results. Therefore, the 1D/2D approach is used to gain rough information about the component geometry and fluid-dynamic behaviour. This allows several options to be quickly compared and, after a preliminary selection, an initial guess configuration can be subjected to the CFD analysis.

In the present study, the procedure adopted for the design of each turbomachine stage is shown in detail in the block diagram reported in Figure 3. Component design data and information regarding major geometric and kinematic parameters, derived from the 0D analysis, are utilized in the 1D preliminary design. Moreover, specific mechanical and aerodynamic constraints, as well as other technical information (eg, materials, bearings, electric machines and gears), are implemented for each component. Preliminary 1D component design aims at determining the most relevant geometrical dimensions,

as well as average kinematic and thermodynamic variables at the main stations. Moreover, a rough value for the major overall performances (exchanged work and efficiency) can be evaluated to select the best design options for each component. The 1D design process is iterative: for ease of reading, such iterations are not reported in the block diagram (blue block). At this stage, the tool interacts with specific databases which contain the working fluid thermodynamic properties and loss correlations for each type of machine. Once a satisfactory preliminary design is achieved, a detailed 3-D geometry of the impeller/rotor is created, meshed and analysed at the nominal point using the commercial CFD software ANSYS-CFX. If the detailed fluid dynamic behaviour is acceptable the diffuser/nozzle is designed, coupled with the impeller/rotor, then analysed. Otherwise, the geometry is updated and the procedure repeated. After each design block, a check is done to verify that the anticipated component performances are in line with the boundary conditions imposed by the initial RCBC optimization. If such conditions are not satisfied, the geometry is modified accordingly, at the most appropriate level.

If this procedure delivers a component that meets plant needs in terms of overall performance, the design is considered completed.
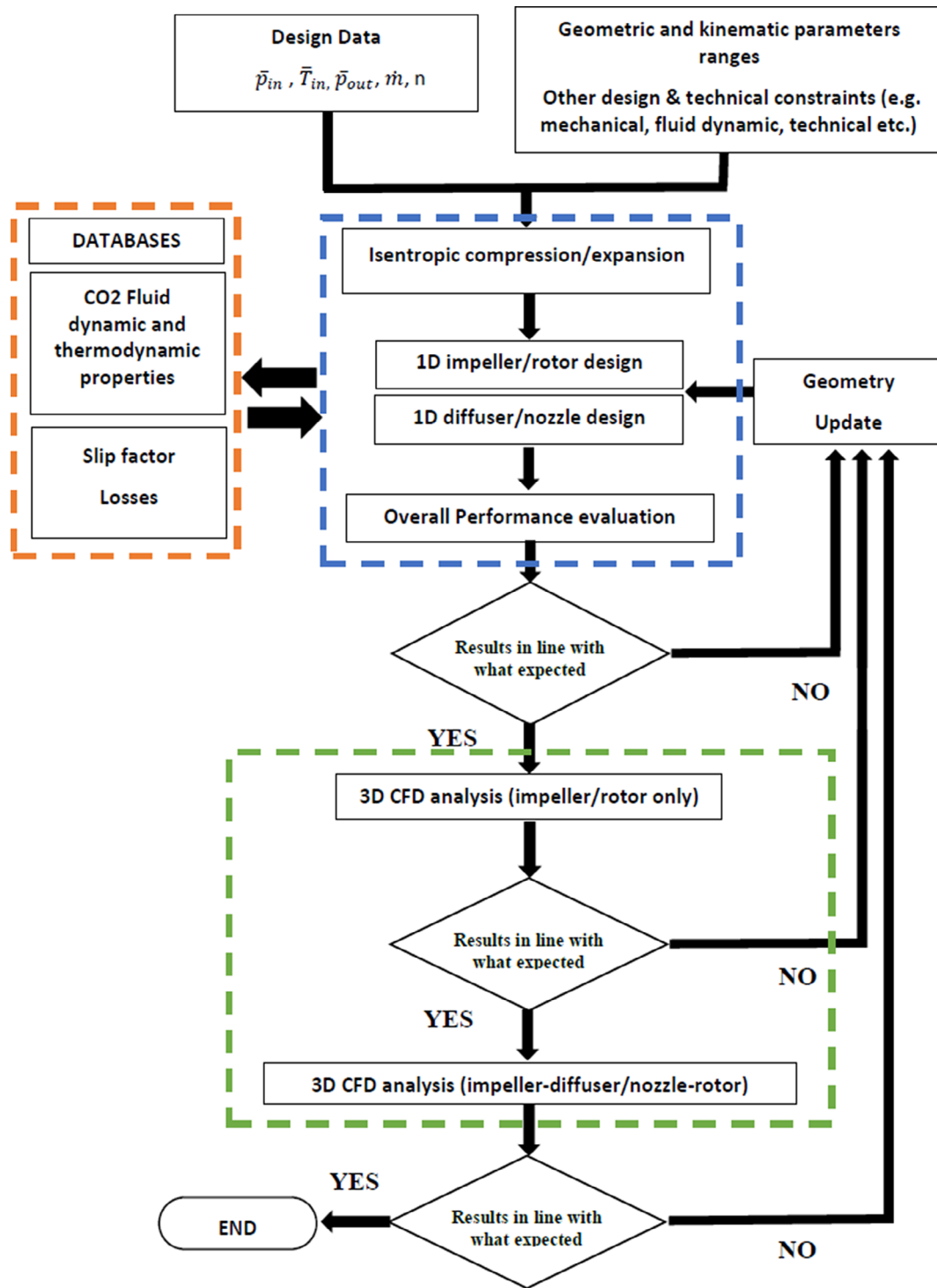
**FIGURE 3** Design procedure block diagram [Colour figure can be viewed at wileyonlinelibrary.com]

## 3.1 | 0D models

The application of the similitude theory is the first step in the component design process. The preliminary selection of shaft speed, types of components, number of stages and reference diameters was completed by applying similarity rules based on Baljes's charts.[30,31] Such charts report general information (ie, main geometry parameters and performance) for well-designed axial and radial turbomachines in terms of two independent parameters, the specific diameter ($D_s$) and the specific speed ($n_s$), which are reported in Equations (1) and (2), respectively:

$$D_s = \frac{DH^{1/4}}{V^{1/2}} \qquad (1)$$

$$n_s = \frac{nV^{1/2}}{H^{3/4}} \qquad (2)$$

$D$ being a reference diameter for the geometric similitude, $V$ the volumetric flow and $H$ the head.

Such charts, as well as their variants in the literature, were produced by applying the similitude theory. Secondary effects, such as compressibility (Mach number), turbulence (Reynolds number) and working fluid reality, which affect and modify the charts, are neglected in the first stage of the design process because of the high level of uncertainty; such effects are taken into consideration during the 1D analysis, and mainly in the following 3D detailed numerical study.

## 3.2 | 1D models

The 1D preliminary design was performed using two in-house tools – one for centrifugal compressors and the other for radial-inflow expanders – developed in Fortran 90 for S-CO$_2$ turbomachinery. These tools use conservation equations, relations for the mean-line velocity diagrams, and the Euler's equation to perform the design and evaluate average working fluid thermodynamic states at the main sections (ie, the inlet/outlet sections of impeller/rotor and diffuser/nozzle). To estimate stagnation and static thermodynamic properties of the working fluid, a specific database was set up using REFPROP v9 data.[32]

Semi-empirical correlations were adopted for the estimation of the slip factor and major losses (ie, aerodynamic, recirculation, leakage, disk friction).

The slip factor ($\sigma$) reflects the imperfect working fluid guidance inside the impeller (centrifugal compressors) and rotor (radial turbines), which reduces the exchanged work and modifies the average fluid direction at the impeller/rotor exit. In design problems, it is applied for the preliminary prediction of the mean-line exit blade angle. Stodola's correlation[33] was used for compressor impellers, since most of the recent correlations were derived experimentally for turbomachines operating with conventional fluids (air or steam) and there is no evidence in the literature of their reliable application for unconventional fluids, as the one used in the present case study. For radial-inflow turbines, the Augier's simplified equation[34] was taken into consideration.

For centrifugal compressors, fluid-dynamic losses were considered and computed by means of an internal efficiency, which is evaluated in terms of n$_s$ and D$_s$, according to Balje's charts. For radial turbines, fluid dynamic losses in rotors and nozzles were calculated using relations reported in[35,36] in terms of velocity coefficients (flow exit velocity divided by isentropic exit velocity – $\phi_R$ and $\phi_N$). Such coefficients were selected in the conventional range of well-designed radial machines.

Moreover, for compressor stages, other losses were included in the model. In particular:

- Disk friction losses, which result from the work transferred by the impeller to the fluid in the secondary path, between the cover disk and the shroud [Equation (4)]:
- Leakage losses related to the recirculation of the secondary flow in the impeller passage [Equation (6)]. The gap between shroud and casing (g) was assumed 0.5 mm.
- Skin friction losses [Equation (10)] and mixing losses [Equation (12)] were added for stages equipped with a vaned diffuser.

Other aerodynamic losses in the stationary parts due to incidence effects and non-uniformity in the velocity distribution into the path were neglected at this stage, but considered in detail in 3-D simulations.

In addition to the abovementioned slip factor effect and fluid dynamic losses, windage losses were evaluated by Equation (22) for radial-inflow expanders' stages.

All the semi-empirical correlations implemented in the 1D models are reported in Table 2.

## 3.3 | CFD models

Once each component was preliminary designed, the numerical CFD three-dimensional analysis at the design point was carried out using the commercial-available software ANSYS-CFX. As the final goal of the analysis was the estimation of the components' nominal performance, quasi-steady analyses were conducted. To reduce computational and time efforts, a small number of blade/vane channels were modelled, taking advantage of the radial symmetry of the machines. Therefore, periodic boundary conditions were set.

A structured H—O—H three-dimensional mesh was generated for both compressors and expanders. Appendix A reports the major mesh quality parameters (maximum and minimum face angles, edge length ratio, element volume sizes) for the final meshes; all were within the recommended ranges.

For compressors stages equipped with a vaned diffuser or radial turbines with nozzles, a multiple frame

**TABLE 2** Loss correlations implemented in the 1D tool

| Component | | Correlations | Equation no. |
|---|---|---|---|
| Centrifugal compressors | Slip factor ($\sigma$) | $\sigma = \frac{c_{2u'}}{c_{2u'}} = 1 - \frac{\pi}{Z_g} \frac{\operatorname{sen}(\beta_{2c})}{1 + \varphi_2 \operatorname{cotg}(\beta_{2c})}$ | (3) |
| | Fluid-dynamic losses | $\eta = \eta$ (ns, Ds) from Baljie's charts | |
| | Disk friction losses[37] | $\Delta h_{\mathrm{DF}} = f_{\mathrm{DF}} \frac{\left(\frac{\rho_2 + \rho_1}{2}\right) D_{\max}{}^2 u_{\max}{}^2}{16m}$ | (4) |
| | | where, $f_{\mathrm{DF}} = \frac{2.67}{\mathrm{Re}_{\mathrm{DF}}^{0,5}}$, $\mathrm{Re}_{\mathrm{DF}} < 3 \times 10^5$ | (5) |
| | | $f_{\mathrm{DF}} = \frac{0.0622}{\mathrm{Re}_{\mathrm{DF}}^{0,2}}$, $\mathrm{Re}_{\mathrm{DF}} > 3 \times 10^5$ | |
| | | being $\mathrm{Re}_{\mathrm{DF}}$ the Reynolds number evaluated at the impeller exit | |
| | Leakage losses[38] | $\Delta h_{\mathrm{LL}} = \frac{m_{\mathrm{LL}} u_{\mathrm{LL}} u_2}{2m}$ | (6) |
| | | being $m_{\mathrm{LL}}$ the lost mass flow rate and $u_{\mathrm{LL}}$ the fluid velocity through the seals. $u_{\mathrm{LL}}$ can be calculated as | |
| | | $u_{\mathrm{LL}} = 0,816\sqrt{\frac{2\Delta p_{\mathrm{LL}}}{\rho_2}}$ | (7) |
| | | $\Delta p_{\mathrm{LL}} = \frac{m(D_2 c_{2u} - D_1 c_{1u})}{z_G L_b \left(\frac{D_1 + D_2}{2}\right)\left(\frac{b_1 + b_2}{2}\right)}$ | (8) |
| | | $m_{LL} = \rho_2 z_G g L_b u_{\mathrm{LL}}$ | (9) |
| | | where $g$ is the gap between shroud and casing | |
| | Skin friction losses[39] | $\Delta h_{\mathrm{SF}} = 2C_f \frac{L_b}{D_h} \underline{c}^2$ | (10) |
| | | where $c$ is the averaged velocity and $C_f$ is the skin friction coefficient calculated as | |
| | | $\frac{1}{\sqrt{4C_f}} = -2\left(\frac{2,51}{\mathrm{Re}_{D_h}\sqrt{C_f}}\right)$ | (11) |
| | Mixing losses[40] | $\Delta h_{\mathrm{MIX}} = \frac{1}{1 + \tan^2\alpha_2}\left(\frac{1 - \varepsilon_{\mathrm{wake}} - \frac{b}{b_2}}{1 - \varepsilon_{\mathrm{wake}}}\right)\frac{c_2^2}{2}$ | (12) |
| | | being $\varepsilon_{\mathrm{wake}} = 1 - \frac{c_{m,\mathrm{wake}}}{c_{m,\mathrm{mix}}}$ | (13) |
| | | $c_{m,\mathrm{wake}} = \sqrt{c_2^2 - c_{2u}^2}$ | (14) |
| | | $c_{m,\mathrm{mix}} = c_{2m}\delta_2$ | (15) |
| Radial-inflow turbines | Slip factor ($\sigma$)[34] | $\sigma = 1 - \sqrt{\operatorname{sinsin}\beta_3}/N_R^{0.7}$ | (16) |
| | | being | |
| | Number of blades Rohlik[41] | $N_R = 12 + 0.03\,(33 - \alpha_3)^2$ | (17) |
| | Rotor friction losses[35] | $\zeta_R = \frac{1}{\varphi_R^2} - 1$ | (18) |
| | | being $\varphi_R$ the velocity coefficient | |
| | | $\varphi_R = \frac{w_3}{w_{3is}}$ | (19) |
| | Nozzle friction losses[35] | $\zeta_N = \frac{1}{\varphi_N^2} - 1$ | (20) |
| | | being $\varphi_N$ the velocity coefficient | |
| | | $\varphi_N = \frac{c_2}{c_{2is}}$ | (21) |
| | Windage losses[42] | $\Delta h_w = \frac{0.56\,\rho_2 D_2^2 \left(\frac{U_2}{100}\right)^3}{\cdot m\,Re}$ | (22) |

approach was applied; the flow was assumed to be steady in the proper frame of reference (stationary or moving). In moving sub-domains, which are not inertial ones, some additional terms like centrifugal and Coriolis forces were added into the momentum equation. The interface between adjacent sub-domains was treated using the "frozen rotor" technique, which provides a local coupling between adjacent stationary and moving sub-domains.

A grid independence analysis was carried out for each case (impeller/rotor, compressor/expander stage), and the mesh refined accordingly. Simulations for geometries discretized in structured meshes refined from $1.5 \times 10^5$ to $2 \times 10^6$ nodes per channel were carried out. Stabilized results were found for meshes with $3 \times 10^5$ to $4.7 \times 10^5$ nodes in all cases, except for the MC. For such a machine, which works close to the critical point, a more accurate geometry discretization was necessary; the grid independence analysis led to a minimum mesh refinement of $5.5 \times 10^5$ nodes per channel.

To perform steady-state 3D viscous flow simulations, the discretization of Navier-Stokes equations was realized using a high-resolution advection scheme. To simulate expanders' stages, the standard $k$-$\varepsilon$ turbulent model

with scalable wall function was selected. Such a model is stable and offers a good compromise in terms of accuracy and numerical robustness. Several authors have already applied the $k$-$\varepsilon$ model to S-CO$_2$ turbine numerical analysis.[20,43] Although standard two-equation models, such as the $k$-$\varepsilon$ one, provide reasonable predictions for many flows of engineering interest, they could not provide enough accuracy for the simulation of flows with boundary layer separation as in radial compressors. So, the $k$-$\varepsilon$ SST (Shear-Stress-Transport) model was chosen to model the main compressor and the recompressor. The SST model accounts for the transport of the turbulent shear stress and it usually gives accurate predictions of the flow separation under adverse pressure gradients.[44,45]

The properties of the working fluid were determined by using the Aungier-Redlich-Kwong model.[46] This model is based on a simple cubic equation that requires a reduced amount of information to be applied (critical WF properties and an acentric factor). In the formulation modified by Aungier,[46] the equation of state is robust and accurate for fluids close to their critical point, although it is not applicable for compressed liquids.

A more accurate model was implemented in the case of the MC using the REFPROP database,[32] since the flow could be saturated. If a biphasic mixture appears locally inside the machine, both liquid and vapour phases are considered by means of the Euler/Euler approach. This approach considers a homogeneous mixture of both phases, and – from a numerical point of view – source terms are added in the Navier-Stokes equations system to account for mass transfer between liquid and gas. For the gas phase, instead, only the continuity equation needs to be specified. More details are reported in.[47]

For each case analysed, the normalized residuals were monitored and convergence criteria for them were set lower than $10^{-4}$.

Sensitivity analyses were carried out at the end of the design process for each geometry which was found suitable for satisfying optimized RCBC boundary conditions. According to detailed fluid-dynamic results, several relevant geometric parameters were varied to allow for the reduction of local stalls. In particular:

- Number of blades/vanes;
- Thickness and thickness distribution from leading to trailing edge of blades and vanes;
- Meridional shape of shroud profiles;
- Blades' height at impeller/rotor inlet/exit sections;
- Impeller exit blade angle for compressor stages;
- Absolute inlet angle for expander stages;

- Blade angle variation through the path at hub and tip lines (for impellers/rotors).

Numerical results achieved using the above-mentioned models can be considered sufficiently reliable for the design of S-CO$_2$ radial turbomachines. Previous literature has demonstrated that conventional numerical models for turbulence and gas properties, like those applied in this study, and even simpler ones (eg, Spalart-Allmaras one-equation turbulence model), can be successfully compared with experimental results.[48] More attention needs to be paid to performance evaluation of compressors working close to the critical point. For such machines, general gas properties need to be replaced with detailed databases (like REFPROP). If the fluid properties are calculated accurately, even mean-line models can yield acceptable results.[49] The deviation between experimental tests and CFD results can be mainly attributed to the role of parasitic losses (leakage and disk friction), which are relevant in small machines for high-density fluids like S-CO$_2$.[50] Parasitic losses are not computed in CFD analysis thus, in this study, they were calculated separately and considered when evaluating component performance.

A design process such as the procedure applied in this study, based on both average mean-line models and CFD simulations, can provide more reliable results than those based on a single method because a constant results comparison can be made. The application of CFD simulations alone could lead to a performance overestimation.

In the following section, final results for each component of the power-block configurations 2b and 2c (Figure 3) obtained using the process described in this chapter are reported and discussed.

# 4 | RESULTS AND DISCUSSION

The design procedure was, first, applied to the simplest conceptual configuration scheme reported in Figure 2A. The MC and the RC are the most challenging components and considerably affect the layout and design of the whole system. One of the main reasons is that the MC works in transcritical conditions at the inlet section, and, as a result, the WF properties change dramatically during the compression process. Accordingly, the final design of the MC could differ significantly from the preliminary one. A second issue is related to the RC small mass flow rate (one third of the overall flow); this entails several concerns for the simultaneous assessment of major thermodynamic and mechanical design

constraints. Based on,[51] the following constraints were taken into consideration in the preliminary design of the compressors:

- Geometric and kinematic parameters at the impeller inlet section (MC and RC stages): the ratio of hub to tip diameter ($\chi_1$), the tip blade angle ($\beta_{1c}$), and the ratio of impeller axial to radial length;
- Geometric and kinematic parameters at the impeller exit section: the ratio of peripheral absolute velocity to impeller speed (stage load coefficient $-\psi_2-$), the ratio of the blade height to the impeller diameter, and the ratio of impeller exit diameter to mean-line inlet diameter ($\chi_2$);
- Mechanical constraints related to the maximum transmissible torque for each stage, which leads to a minimum shaft diameter fixing shaft speed, materials, and machining techniques. At this stage, rotodynamic and fatigue effects were neglected.

In this study, MC and RC designs vary significantly according to shaft speed. Indeed, keeping the machine pressure ratio constant, the lower the shaft speed, the higher the number of stages, and the higher the mechanical torque. The value of the torque poses several constraints to the geometry of the impeller inlet section. Table 3 shows the suitable number of stages for MC and RC as the shaft speed varies. Such data were carried out using Balje's charts. A shaft speed between 15 000 and 35 000 rpm was selected on the basis of the previous literature. Depending on shaft speed and the placement of the components, the MC can be a one or two-stage compressor, while the RC can be a one-, two- or three-stage machine. Other possible arrangements were discarded because of mechanical or aerodynamic issues.

All options reported in Table 3 were designed at the 1D level using the tool CO2DES. Finally, the configuration with the fewest stages and all design parameters in accordance with the best practice values was designed

and analysed in detail. The tentative shaft speed was set at 25 000 rpm, so a one-stage MC and a two-stage RC were designed.

## 4.1 | Recompressor (RC)

Each stage was equipped with a vaned diffuser. Impellers and diffusers were iteratively designed according to the procedure presented in Figure 3. The main parameters for the preliminary design of each stage are reported in Table B1 in Appendix B, while preliminary 1D and final results are compared in Table B2. Figure 4A shows the final RC first stage geometry and Figure 4B shows the mean-line velocity contours, while Figure 5 reports the final second-stage impeller. In addition, velocity contours for the preliminary and final second-stage geometries are given in Figures 6 and 7, respectively. In Figure 6, stalls and eddies are clearly visible in the preliminary geometry from mean-line to tip-line. In Figure 7, the local fluid-dynamic behaviour was significantly improved following the iterative design process discussed above. As a result, the stall region was dramatically reduced, increasing the performance of the RC.

Tables 4 and 5 present the major results (eg, pressure ratio, internal efficiency, power) for both preliminary and final geometries at the nominal point. The overall pressure ratio of the RC was not equally distributed between the stages in the preliminary design. This was due to the low volumetric flow rate at the second stage, which imposed several constraints on the impeller geometry. During the iterative design process, it was possible to mitigate the aforementioned aspect, and balance the RC stages.

## 4.2 | Main compressor (MC)

A one-stage MC was initially modelled as discussed above. The preliminary geometry is reported in detail in.[27] Applying the 1D models described in Section 3.1, a centrifugal stage made of a shrouded impeller and an unvaned diffuser was designed.

Although the 1D design was successfully completed, the 3D numerical analysis revealed a relevant $CO_2$ liquid fraction inside the MC impeller close to the elbow (about 20 wt%) due to high local velocities. The phase change modified completely the expected WF fluid-dynamic behaviour inside the MC: supersonic flow, shock waves, stalls and eddies occurred in the flow path, reducing dramatically the performance of the MC. In particular, the nominal pressure ratio and efficiency

**TABLE 3** Stage number for each compressor

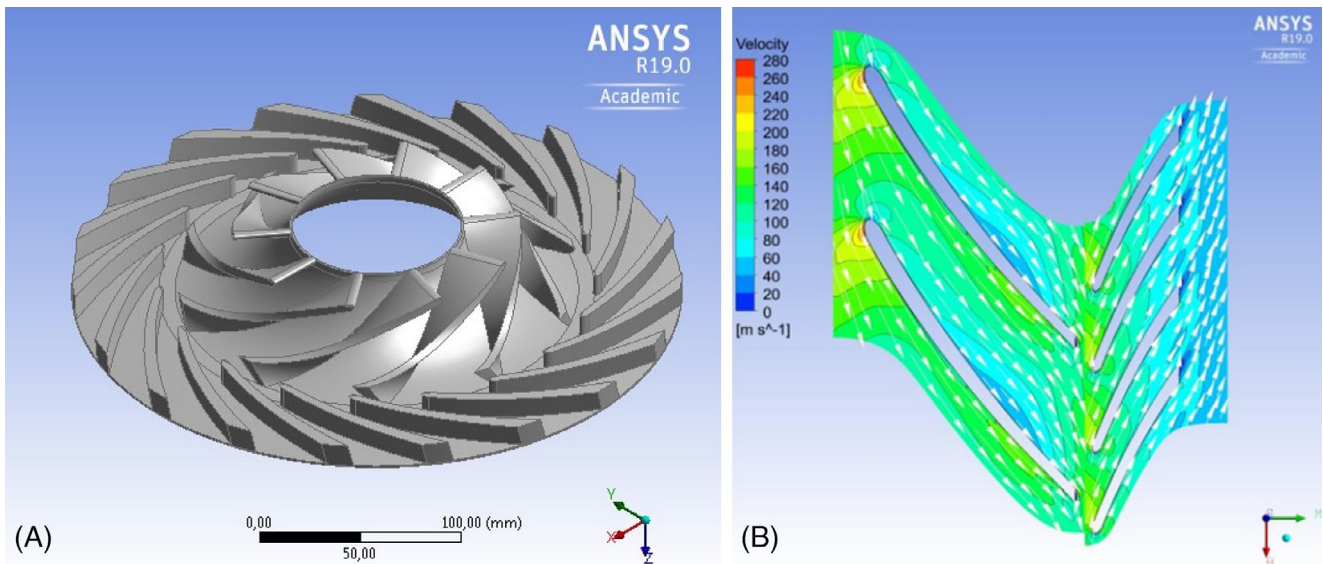|  | Free-standing shaft speed [rpm] | | | |
|---|---|---|---|---|
|  | 30 000 | 25 000 | 20 000 | 15 000 |
| External main compressor | | | | |
| MC | 1 | 1 | 1 or 2 | 1 or 2 |
| RC | 1 | 2 | 2 | 3 |
| External recompressor | | | | |
| MC | - | 1 | 1 | 2 |
| RC | 1 or 2 | 2 | 2 | 3 |

**FIGURE 4** RC 1st stage: A, general overview (the impeller is shrouded); relative and absolute velocities at the mean line for the nominal point [Colour figure can be viewed at wileyonlinelibrary.com]
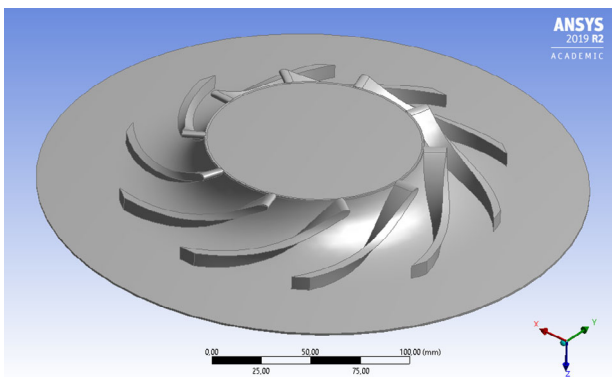


**FIGURE 5** RC 2nd stage: general overview (the impeller is shrouded) [Colour figure can be viewed at wileyonlinelibrary.com]

were significantly lower than expected from the preliminary 1D analysis. As a result, the MC layout was redesigned, splitting the overall pressure ratio between two stages in series.

Two different configurations were considered:

- The two-stage MC layout shown in Figure 2B. In that configuration, the first stage is mechanically decoupled from the high-speed shaft and it is moved by an electric motor at lower speed. The second stage remains unchanged from the previous configuration. Although the overall layout is more complex, the lower speed of the MC first stage can reduce local WF velocities. Thus, it can avoid the fluid condensation at nominal conditions. Moreover, the power-group can have more operational flexibility, since the control system has one

more degree of freedom (the shaft speed of the MC first stage).
- The layout reported in Figure 2C,D, where the MC is de-coupled from the high-speed shaft and moved at low-speed by an electrical motor (Figure 2C) or by the power turbine (Figure 2D). The 0D analysis suggested a re-arrangement of the MC on three centrifugal stages at 7200 rpm to maximize the expected nominal MC efficiency.

In both cases, MC stages were designed using the iterative procedure described in Section 3. All of them are centrifugal stages.

### 4.2.1 | Configuration 2b: two-stage MC

The 3D view of the MC first stage is shown in Figure 8A, while Figure 9 depicts the blade-to-blade iso-Mach contours at 20%, 50% and 80% of blade height. The final configuration did not present remarkable fluid dynamic concerns from mean-line to tip. A local eddy was detected at hub-line, in the elbow (Figure 9), probably connected with secondary flows, as usual in radial machines. It was not possible to remove completely such a phenomenon applying the design procedure. Conversely, the second stage presented in Figure 8B does not show remarkable stalls at any streamline (Figure 10). In Table 4, overall MC performances are reported for both preliminary and final 3D layouts. Geometrical details are listed and compared in Tables B3 and B4 in Appendix B.
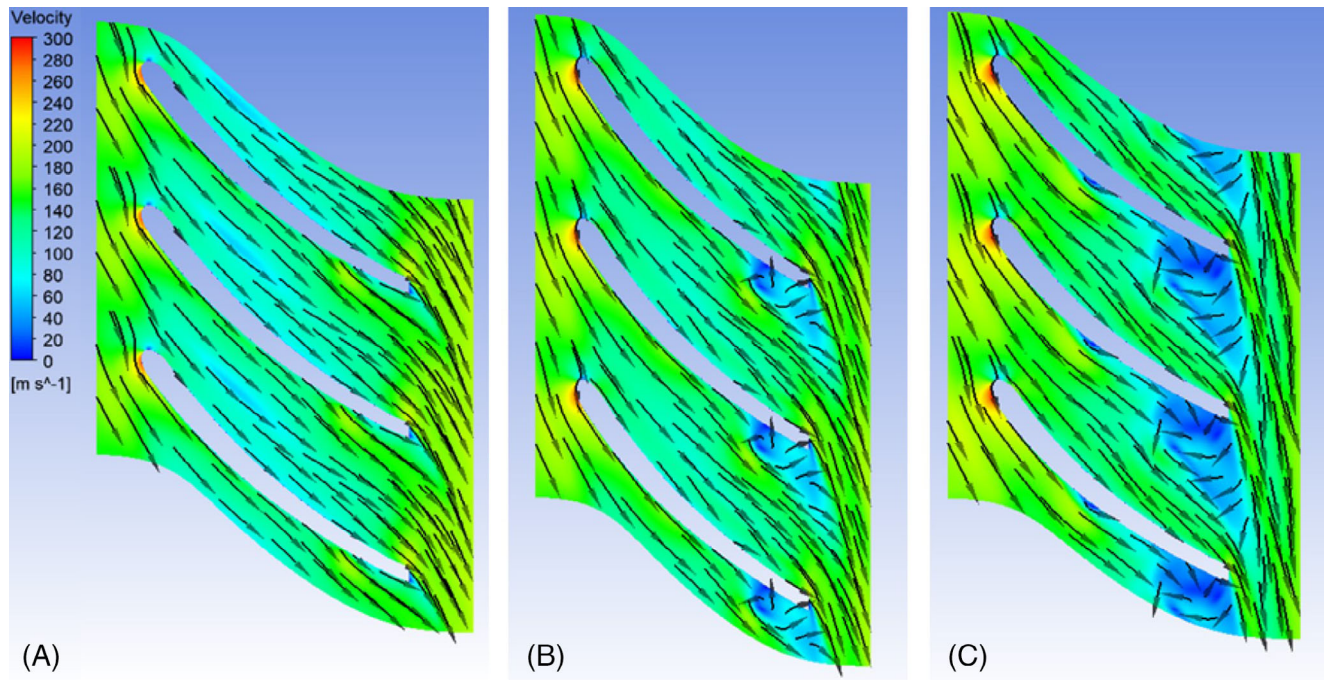
**FIGURE 6** Preliminary design RC 2nd stage: contours of the relative velocity at 20% A, 50% B, and 80% C blade height [Colour figure can be viewed at wileyonlinelibrary.com]
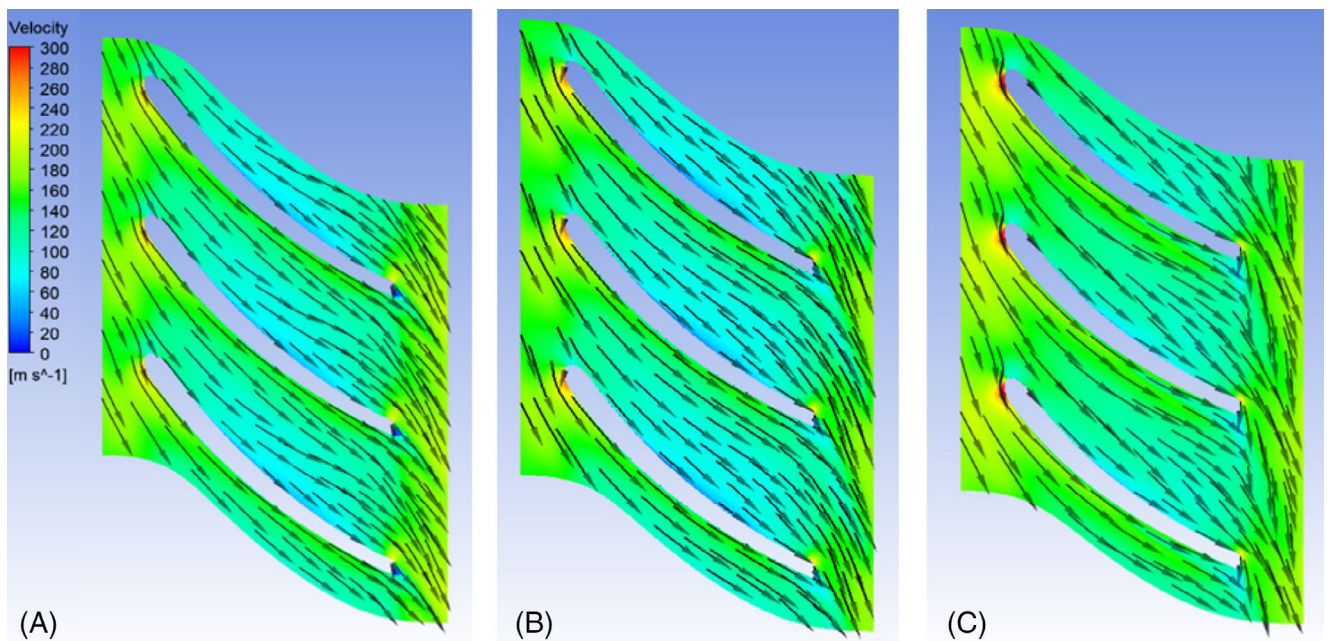


**FIGURE 7** Final design RC 2nd stage: contours of the relative velocity at 20% A, 50% B, and 80% blade height C [Colour figure can be viewed at wileyonlinelibrary.com]

### 4.2.2 | Configurations 2c and 2d: Three-stage MC

tAll the stages in configurations depicted in Figure 2C, D are centrifugal and made of a shrouded impeller, a vaned diffuser, and a return channel between stages. No inlet guide vanes were considered in the design process. The three impellers are reported in Figure 11. Tables B5 and B6 in Appendix B lists the most relevant parameters for preliminary 1D designs and final

**TABLE 4** Configuration 2b: components' performance at the design point

| | RC | | | | MC | | | | EXP1 | | EXP2 | |
| | First stage | | Second stage | | First stage | | Second stage | | | | | |
| | P.G. | F.G. | P.G. | F.G. | P.G. | F.G. | P.G. | F.G. | P.G. | F.G. | P.G. | F.G. |
|---|---|---|---|---|---|---|---|---|---|---|---|---|
| M (kg/s) | 50 | 50 | 50 | 50 | 150 | 150 | 150 | 150 | 200 | 200 | 200 | 200 |
| n (rpm) | 25 000 | 25 000 | 25 000 | 25 000 | 15 000 | 15 000 | 25 000 | 25 000 | 25 000 | 25 000 | 12 000 | 12 000 |
| Pressure ratio | 1.83 | 1.77 | 1.68 | 1.78 | 1.52 | 1.56 | 2.06 | 2.07 | 1.61 | 1.43 | 1.81 | 2.03 |
| Efficiency | 0.9 | 0.95* | 0.87 | 0.94* | 0.8 | 0.95* | 0.83 | 0.91* | 0.84 | 0.87* | 0.85 | 0.89* |
| Power (MW) | 2.35 | 2.08* | 2.45 | 2.6* | 3.9 | 3.5* | 7.8 | 7.2* | 12.7 | 12.8* | 12.7 | 18* |

*Numerical values. Leakage and disk friction losses are evaluated separately.

**TABLE 5** Configuration 2c-d: components' performance at the design point

| | RC | | | | MC | | | EXP1 | | EXP2 | | | |
| | First stage | | Second stage | | First stage | Second stage | Third stage | | | First stage | | Second stage | |
| | P.G. | F.G. | P.G. | F.G. | F.G. | F.G. | F.G. | P.G. | F.G. | P.G. | F.G. | P.G. | F.G. |
|---|---|---|---|---|---|---|---|---|---|---|---|---|---|
| M (kg/s) | 50 | 50 | 50 | 50 | 150 | 150 | 150 | 200 | 200 | 200 | 200 | 200 | 200 |
| n (rpm) | 25 000 | 25 000 | 25 000 | 25 000 | 7200 | 7200 | 7200 | 25 000 | 25 000 | 7200 | 7200 | 7200 | 7200 |
| Pressure ratio | 1.83 | 1.77 | 1.68 | 1.78 | 1.49 | 1.49 | 1.51 | 1.17 | 1.16 | 1.54 | 1.55 | 1.61 | 1.62 |
| Efficiency | 0.9 | 0.95* | 0.87 | 0.94* | 0.96* | 0.95* | 0.95* | 0.90 | 0.94* | 0.90 | 0.97* | 0.90 | 0.97* |
| Power (MW) | 2.35 | 2.08* | 2.45 | 2.6* | 2.68* | 3.7* | 4.41* | 4.9 | 5.1* | 12.6 | 13.9* | 14.8 | 15.3* |

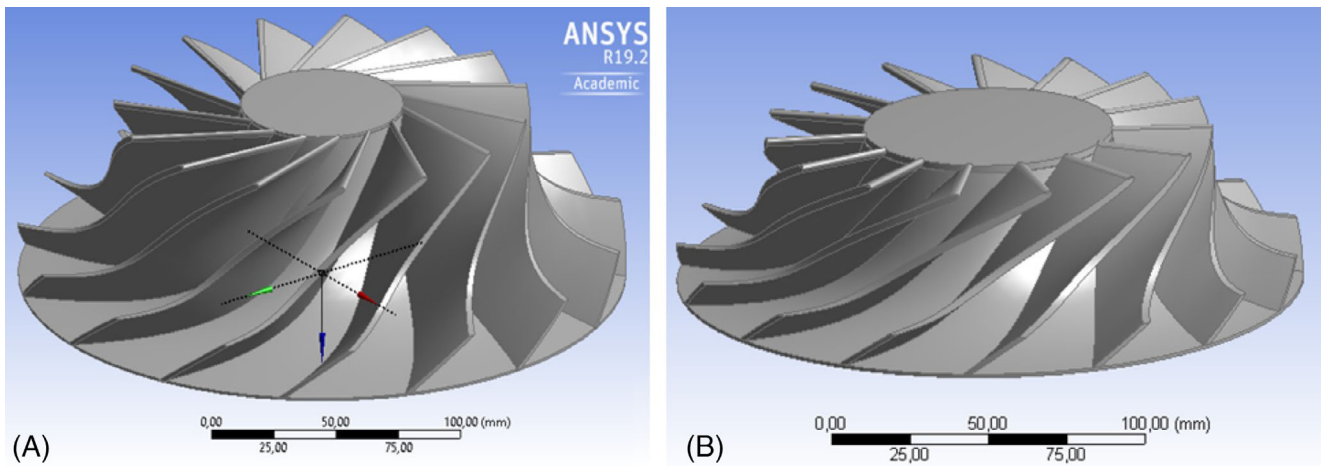*Numerical values. Leakage and disk friction losses are evaluated separately.

**FIGURE 8** Configuration 2b: Details of MC final shrouded impellers. A, first stage; B, second stage [Colour figure can be viewed at wileyonlinelibrary.com]
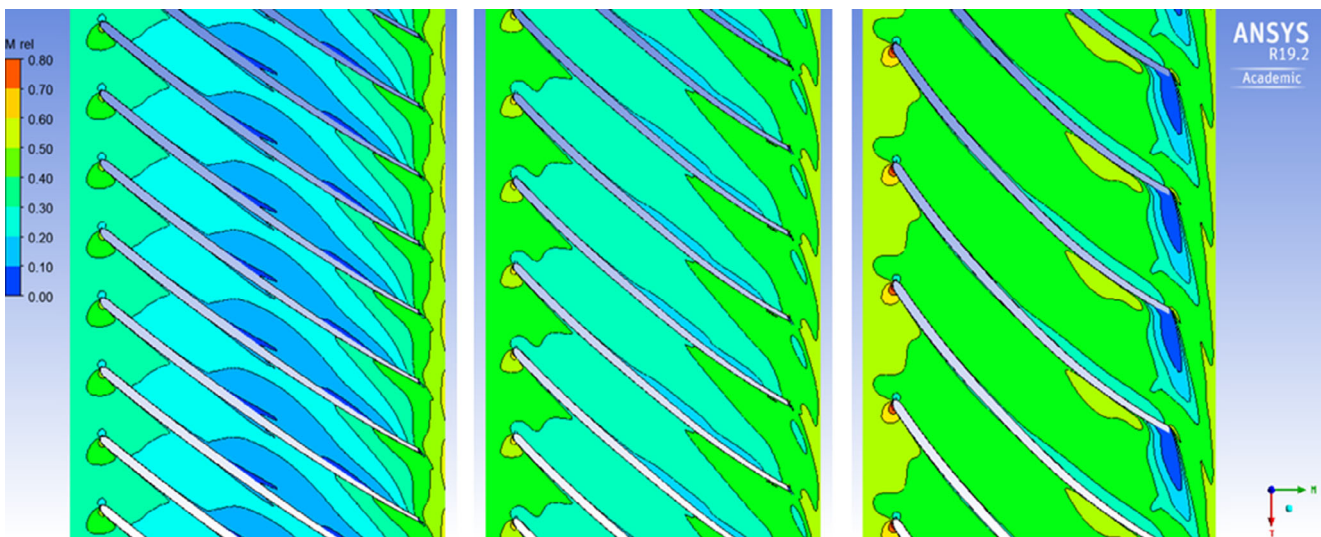


**FIGURE 9** Configuration 2b: MC first stage; relative Mach number at 20%, 50% and 80% of the blade height (from left to right) [Colour figure can be viewed at wileyonlinelibrary.com]
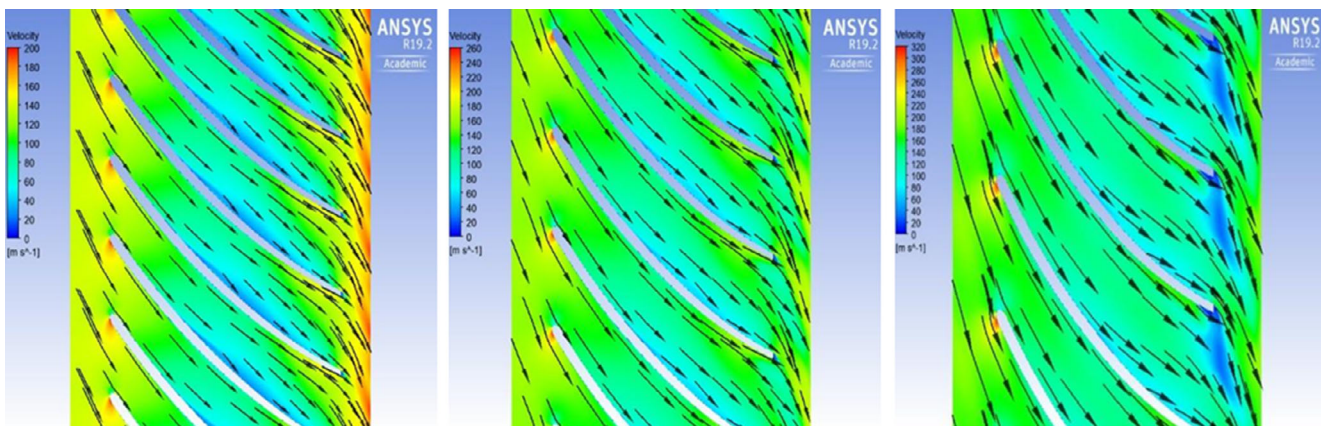


**FIGURE 10** Configuration 2b: MC second stage; contours of relative velocity at 20%, 50% and 80% of the blade height (from left to right) [Colour figure can be viewed at wileyonlinelibrary.com]
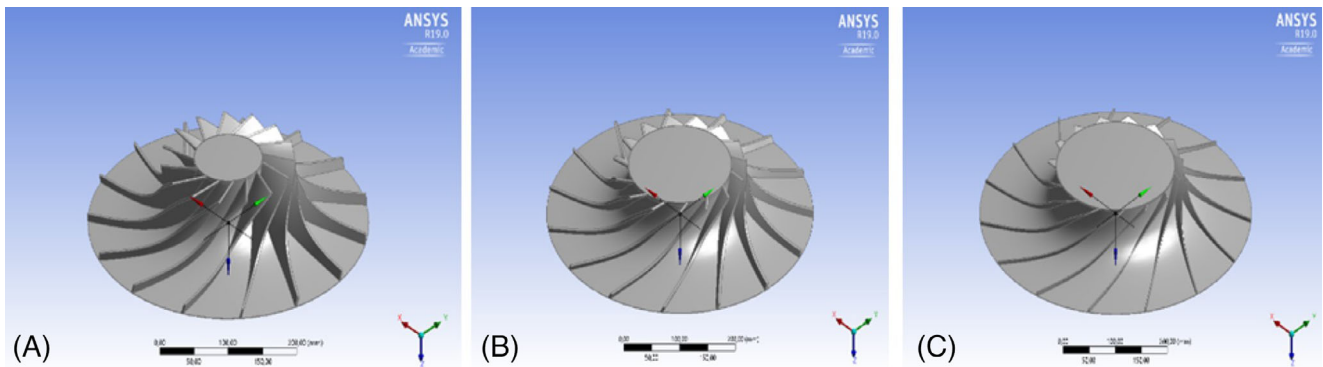
**FIGURE 11** Configurations 2c and d: three-stage MC; impeller details A, first stage; B, second stage; C, third stage [Colour figure can be viewed at wileyonlinelibrary.com]

configurations. As can be noted in Figure 12, the final shapes provide good fluid dynamic behaviour at design conditions. Table 5 reports the final performance for each stage.

## 4.3 | Expanders

After the compressors were modelled, the expanders were designed. In the power-block layouts proposed in Figure 2, the turbine is composed of a high-pressure expander (EXP1) and a low-pressure turbine (EXP2) connected to the electric generator.

### 4.3.1 | Configuration 2b

In Configuration 2b, EXP1 moves the MC second stage and the RC. Therefore, its design was carried out starting from the required nominal power and speed at the nominal mass flow rate. A radial-inflow one-stage expander was modelled using the aforementioned procedure. The remaining pressure drop is used by the power turbine (EXP2). The speed of the EXP2 shaft was set high enough to minimize the number of stages, and low enough to reduce disk friction losses and to allow for a reasonable connection with the generator. Finally, a one-stage EXP2 was modelled. Figures 13A and 14A, depict EXP1 and EXP2 rotors, while Figures 13B and 14B report details of mean-line velocity contours for the final layouts. While the flow path of EXP1 did not highlight specific concerns (Figure 13B), EXP2 showed local stalls. It was not possible to remove such a fluid dynamic effect completely by means of the iterative design process. Tables B7 and B8 in Appendix B give the most relevant parameters for both preliminary and final configurations, while Table 4 compares

overall performances before and after the 3D CFD analysis.

### 4.3.2 | Configuration 2c

In Configuration 2c, the EXP1 moves only the RC, since the entire MC is connected with an electric motor at low speed (7200 rpm). Consequently, the design of the expanders EXP1 and EXP2 was modified, reducing the expansion ratio for EXP1 and increasing it for EXP2. The 0D preliminary analysis suggested a modification of the power turbine because of the higher available pressure drop. Thus, the power turbine was completely re-designed as a two-stage radial-inflow machine to satisfy the specifications of the Balje's chart. In this configuration, the rotors are shrouded and equipped with unvaned nozzles. Figure 15A shows a view of the final EXP1 rotor for the configurations reported in Figure 2C,D. The CFD analysis at nominal conditions did not highlight fluid dynamic issues at any streamline (see Figure 15B). Figure 16 provides details of the EXP2 rotors (first and second stage). As shown in Figures 17 and 18, the flow cannot follow the channel profile perfectly. As observed chiefly in the first stage, incidence losses are coupled with a profile stall. Nevertheless, such phenomena, usual in radial machines, do not significantly reduce the stage performance (see Table 5).

In summary, the design results suggest that configurations 2b and 2c-d are feasible from the point of view of thermodynamics and fluid dynamics. Evaluating disk friction and leakage losses by equations reported in Table 2, and mechanical and electrical losses as suggested in the literature, it was possible to calculate expected global performance for both configurations at the nominal point. Finally, Configuration 2b showed an overall
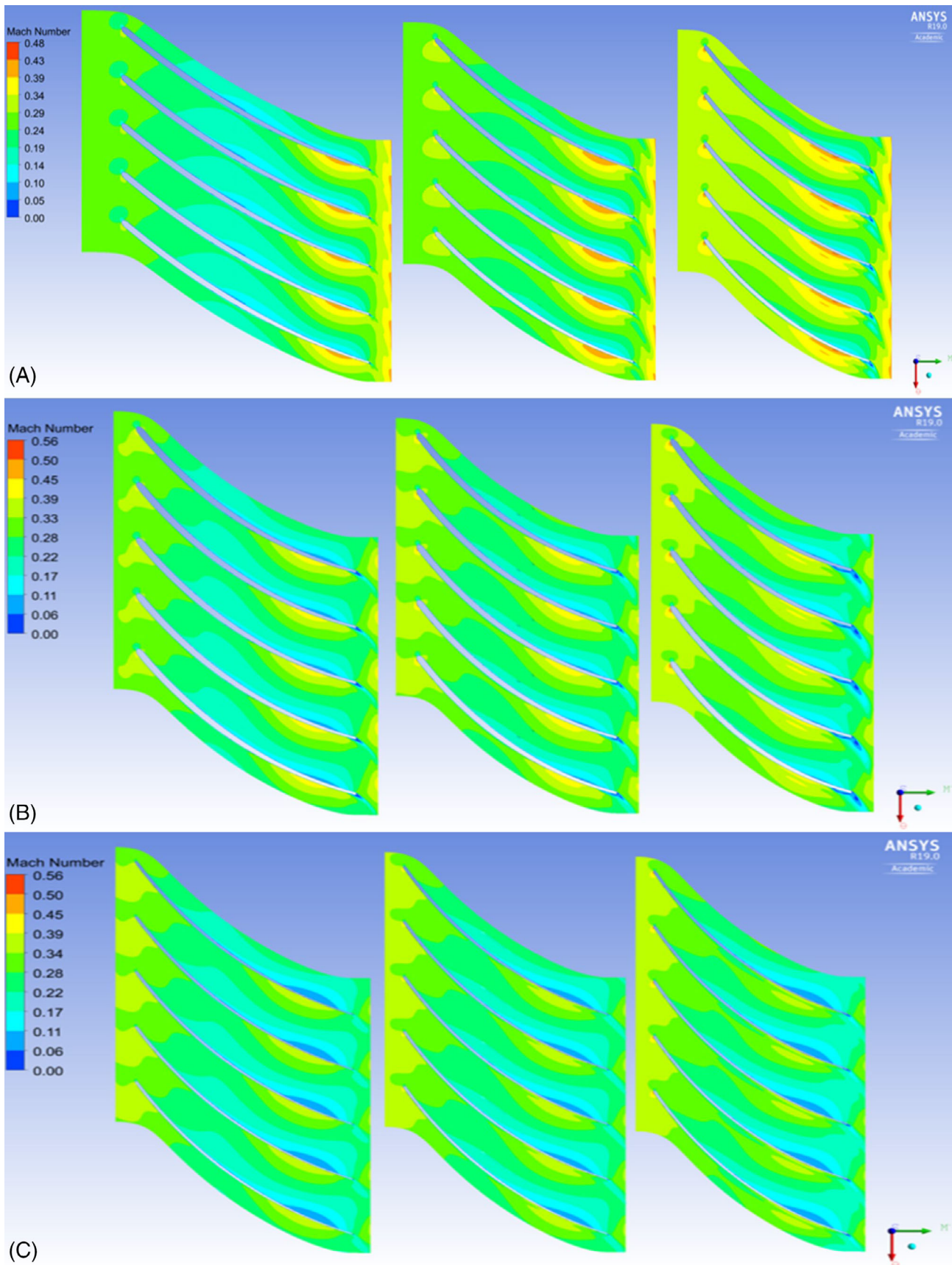
**FIGURE 12** Configurations 2c and 2d: three-stage MC; iso-Mach contours at 20%, 50% and 80% of the blade height (from left to right) for the three impellers A, first stage; B, second stage; C third stage [Colour figure can be viewed at wileyonlinelibrary.com]
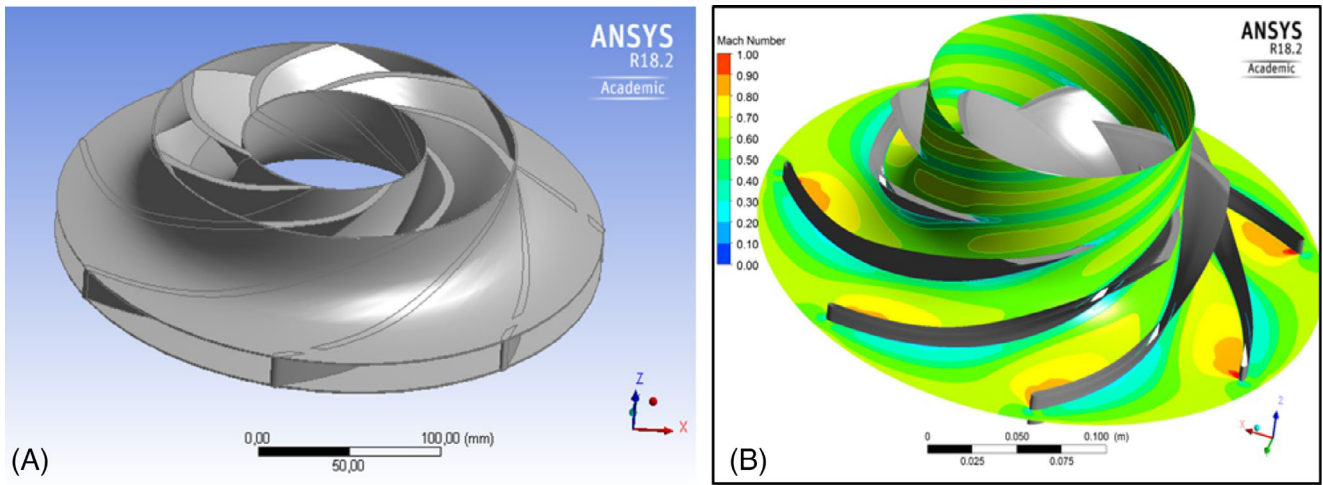
**FIGURE 13** Expander EXP1: A, rotor overview; B, velocities at the mean line [Colour figure can be viewed at wileyonlinelibrary.com]
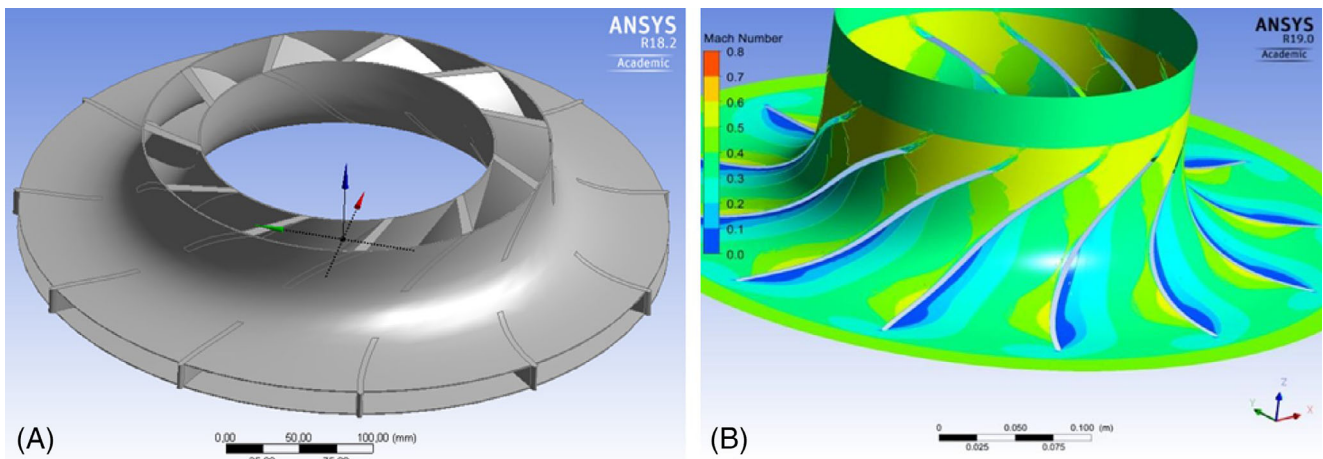


**FIGURE 14** Power turbine: A, rotor overview; B, relative Mach number at the mean line [Colour figure can be viewed at wileyonlinelibrary.com]
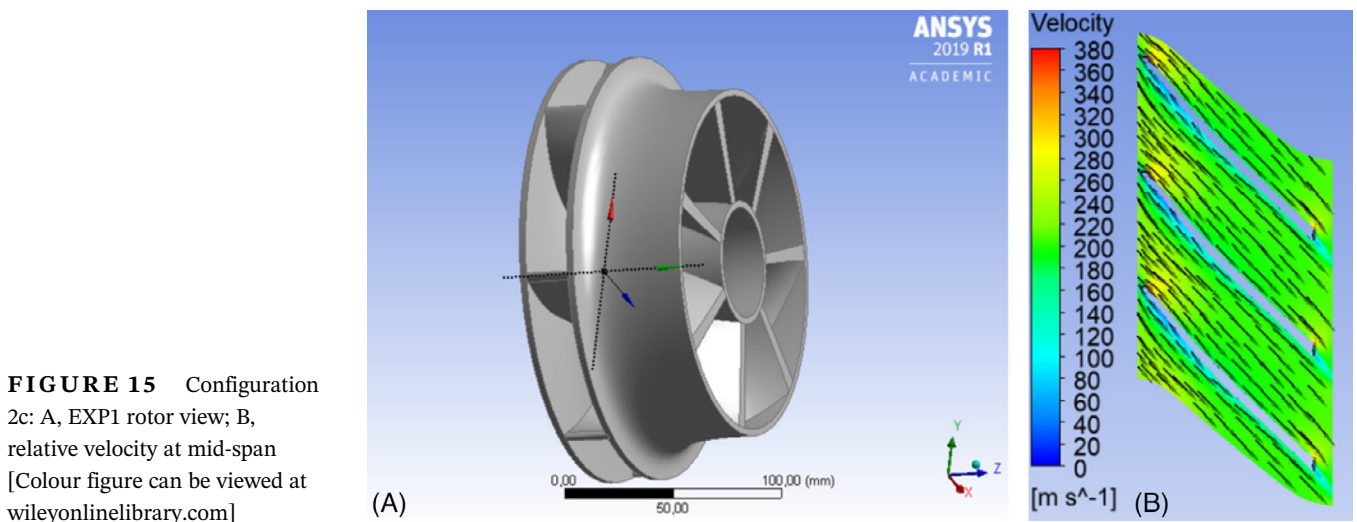
**FIGURE 15** Configuration 2c: A, EXP1 rotor view; B, relative velocity at mid-span [Colour figure can be viewed at wileyonlinelibrary.com]
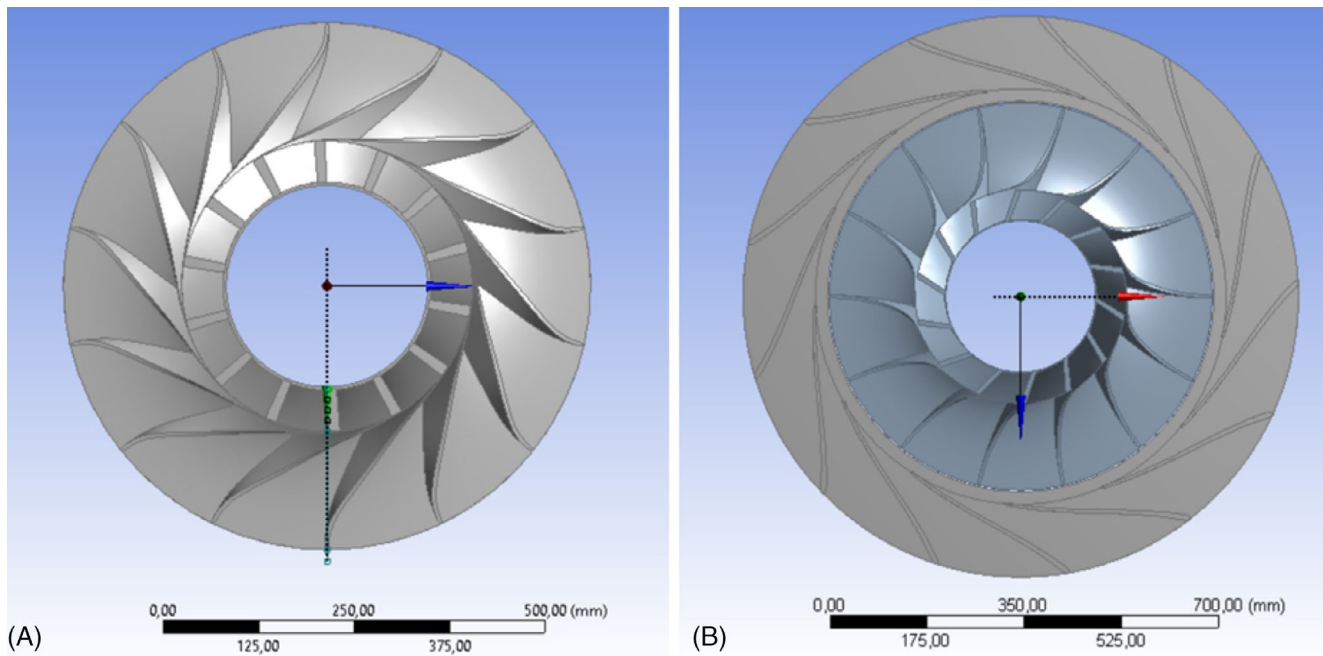
**FIGURE 16**    Configuration 2c: EXP2 rotor views A, first stage; B, second stage [Colour figure can be viewed at wileyonlinelibrary.com]



**FIGURE 17**    Configuration 2c: EXP2 first-stage contours of relative velocity at 20%, 50% and 80% of the blade height (from left to right) [Colour figure can be viewed at wileyonlinelibrary.com]

power output of almost 13.2 MW, which is higher than the power of the configuration 2c (11.7 MW). This difference is largely due to the MC arrangement: in the configuration 2b the velocity of the high-speed shaft enables a reduction in the number of MC stages, allowing for the arrangement of a two-stage machine; conversely, in the configuration 2c the low-speed shaft leads to a three-stage

compressor. In addition, first and second MC stages need to be equipped with vaned diffusers and return channels, which considerably reduce the overall performance of the MC. The selection of the final layout should also take into consideration the overall system flexibility. Thus a careful investigation of the power-block part load behaviour will be carried out.
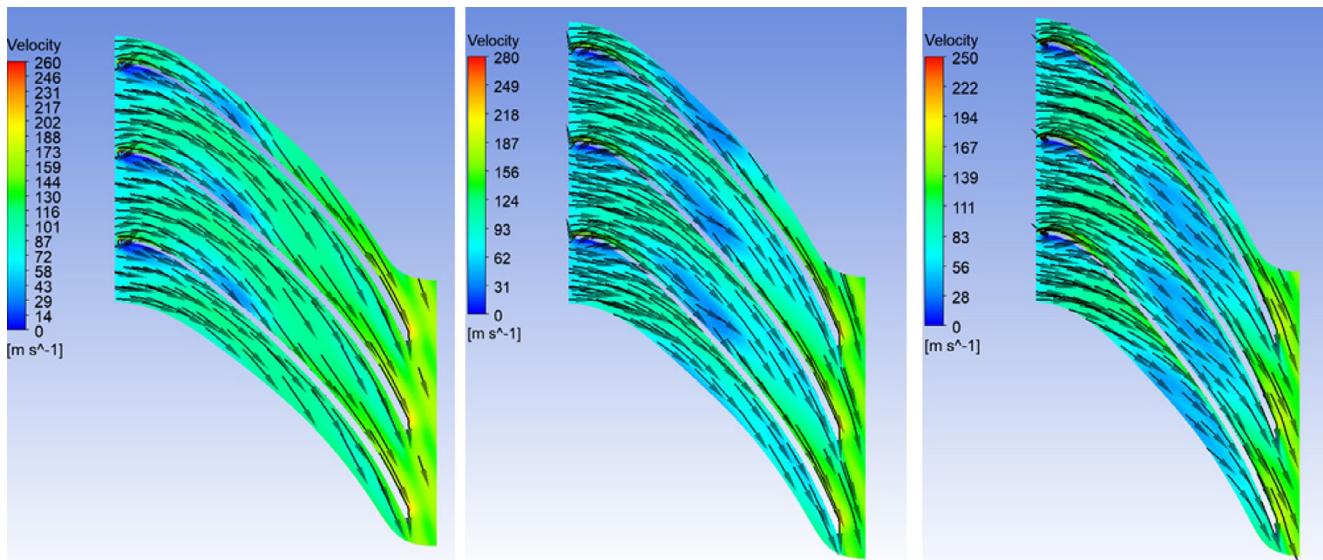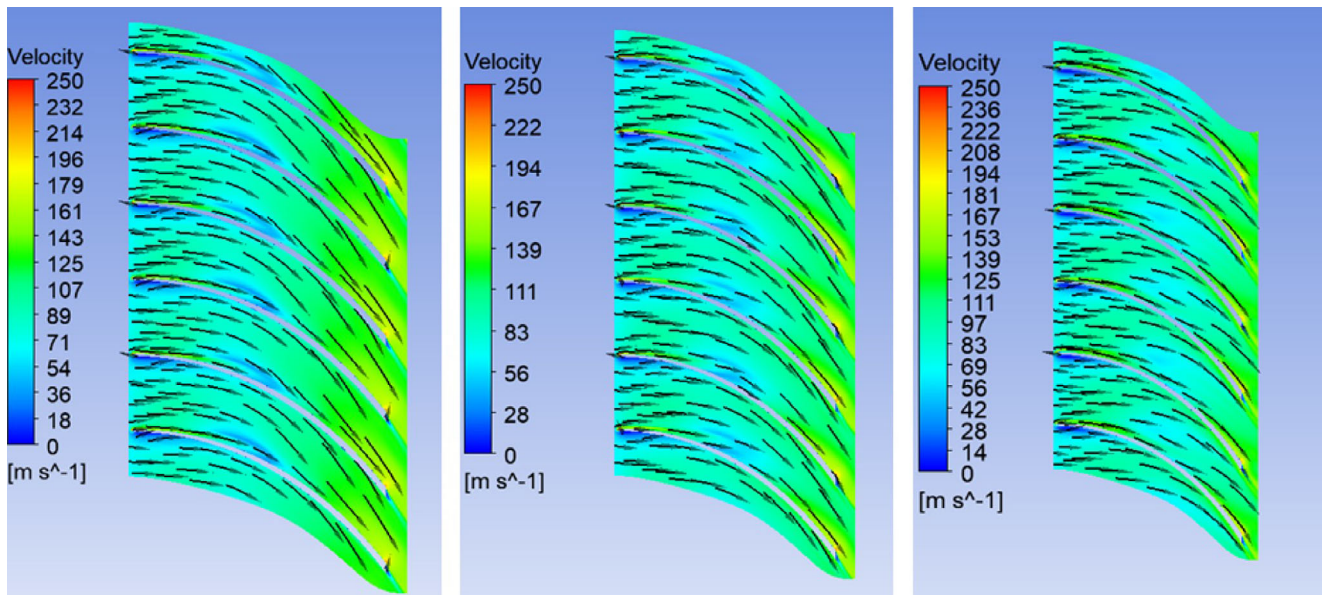
**FIGURE 18** Configuration 2c: EXP2 second-stage contours of relative velocity at 20%, 50% and 80% of the blade height (from left to right) [Colour figure can be viewed at wileyonlinelibrary.com]

## 5 | CONCLUSION

The design of power-blocks for S-CO$_2$ RCBCs poses several concerns. This is due to the novelty of these machines, which use an unconventional working fluid (in terms of thermodynamic and transport properties), at pressures far outside from common gas turbine ranges. Several advancements have been made for large- and small-scale systems. For such scales, multi-stage axial components (compressors and expanders) for large systems, and compact radial machines for small ones were designed and, in some cases, tested at prototype level. At medium scale, the selection of the most relevant parameters (eg, shafts' arrangement, speed, component types and number of stages) dramatically affects the overall layout. Therefore, several power-block layouts are feasible.

In this paper, two power system layouts for an S-CO$_2$ RCBC of ∼10 to 15 MW were modelled. Both of them are innovative compared to conventional gas and steam turbines, as well as to other S-CO$_2$ power systems described in the literature. They were designed from the overall system layout to the sub-components of each machine by means of an iterative procedure, which involves 0D, 1D and numerical 3D models. Starting from almost 22.85 MW (according to the system isentropic analysis) the power-block corresponding to configuration 2b is expected to achieve an overall output power of 13.2 MW. Configurations 2c and 2d should have an output power of 15.6 MW and 16.2 MW, respectively. The different output power among analysed layouts is mainly due to the MC design and supply; in the configuration 2b, the MC second stage was designed for a

shaft speed, which is a trade-off between RC and MC requirements. Conversely, in configurations 2c and 2d MC stages were optimized for a lower shaft speed, reducing aerodynamic losses in both rotary and stationary parts. Moreover, the arrangement 2c could be promising in terms of system flexibility, since the MC is de-coupled from the high-speed shaft and one more degree of freedom in the system control could be added (varying the MC shaft speed). Therefore, further investigations focused on the off-design behaviour of the components and of the whole system will be undertaken to evaluate the best system layout. Components' maps will be implemented in the RCBC simulator to study the flexibility of the power plant and to carry out the plant off-design analysis.

### NOMENCLATURE

| | |
|---|---|
| $b, h$ | blade height |
| $c$ | absolute fluid velocity |
| Cf | skin friction coefficient |
| $D$ | diameter [m] |
| $g$ | gap between shroud and casing |
| $h$ | enthalpy |
| $H$ | head |
| Lb | Channel equivalent length |
| $m$ | Mass flow rate |
| $n$ | shaft speed [rpm] |

| | |
|---|---|
| $p$ | pressure |
| PR | pressure ratio |
| $R$ | gas constant |
| Re | Reynolds number |
| $T$ | temperature |
| $u$ | tangential velocity |
| $v$ | specific volume |
| $V$ | volume flow [m$^3$/s] |
| $w$ | relative velocity |
| Zg, NR | blade number |

## GREEK SYMBOLS

| | |
|---|---|
| $\alpha$ | absolute velocity angle |
| $\beta$ | relative velocity angle |
| $\eta$ | efficiency |
| $\zeta$ | loss coefficient |
| $\rho$ | density |
| $\sigma$ | slip factor |
| $\phi$ | flow coefficient |
| $\chi$ | ratio of hub to tip diameter |
| $\psi$ | stage load coefficient |
| $\omega$ | acentric factor |

## SUBSCRIPTS

| | |
|---|---|
| $c$ | critical, blade |
| DF | disk friction |
| $G$ | impeller |
| in | inlet |
| is | isentropic |
| LL | leakage losses |
| $m$ | meridional |
| max | maximum |
| MIX | mixing losses |
| out | outlet |
| $u$ | tangential component |
| $R$ | rotor |
| $s$ | specific |
| $S$ | stator |
| SF | skin friction |
| $w$ | windage |

## ORCID

*Ambra Giovannelli* 🄳 https://orcid.org/0000-0003-4991-173X
*Coriolano Salvini* 🄳 https://orcid.org/0000-0002-9632-4696

## REFERENCES

1. European Environment Agency, Annual European Union greenhouse gas inventory 1990–2017 and inventory report 2019, EEA/PUBL/2019/051.

2. International Energy Agency, World Energy Outlook 2018, 2018.

3. Bryant JC, Saari H, Zanganeh K, An Analysis and Comparison of the Simple and Recompression Supercritical CO$_2$ Cycles, Supercritical CO$_2$ Power Cycle Symposium, May 24–25, 2011, Boulder, Colorado.

4. Angelino G. Carbon dioxide condensation cycles for power production. *J Eng Power*. 1968;90(3):287-295.

5. Angelino G. Real gas effects in carbon dioxide cycles. Paper presented at: ASME 1969 gas turbine conference and products show, Cleveland, OH

6. Feher E. The supercritical thermodynamic power cycle. *J Energy Convers Manag*. 1968;8:85-90.

7. Feher E, Investigation of supercritical (Feher) cycle. Astropower Laboratory, Missile & Space Systems Division

8. Crespi F, Gavagnin G, Sánchez D, Martínez GS. Supercritical carbon dioxide cycles for power generation: a review. *Int J Appl Energy*. 2017;195:152-183.

9. Dostal V, Driscoll MJ, Hejzlar P. A supercritical carbon dioxide cycle for next generation nuclear reactors. Tech rep MIT-ANP-TR-100 2004: pp. 1–317.

10. Astolfi M, Alfani D, Lasala S, Macchi E. Comparison between ORC and CO$_2$ power systems for the exploitation of low-medium temperature heat sources. *Int J Energy*. 2018;161:1250-1261.

11. Kong F, Li Y, Sa R, Bai Y, Jin M, Song Y. Design and thermodynamic analysis of supercritical CO$_2$ reheating recompression Brayton cyclecoupled with lead-based reactor. *Int J Energy Res*. 2019;43(9):4940-4948.

12. Chen MF, Yamaguchi H, Zhang XW, Niu XD. Performance analyses of a particularly designed turbine for a supercritical CO$_2$-based solar Rankine cycle system. *Int J Energy Res*. 2015;39(13):1819-1827.

13. Zhang XR, Yamaguchi H. An experimental investigation on characteristics of supercritical CO$_2$-based solar Rankine system. *Int J Energy Res*. 2011;35(13):1168-1178.

14. Wang T, Long HA. Techno-economic analysis of biomass/coal Co-gasification IGCC systems with supercritical steam bottom cycle and carbon capture. *Int J Energy Res*. 2014;38(13):1667-1692.

15. Bai Z, Zhang G, Yang Y, Wang Z. Design performance simulation of a supercritical CO$_2$ cycle coupling with a steam cycle for gas turbine waste heat recovery. *J Energy Resour Technol*. 2019;141(10):102001.

16. Chen Y, Wang M, Liso V, et al. Parametric analysis and optimization for exergoeconomic performance of a combined system based on solid oxide fuel cell-gas turbine and supercritical carbon dioxide Brayton cycle. *J Energy Convers Manag*. 2019;186(15):66-81.

17. Roy D, Samanta S, Ghosh S. Thermo-economic assessment of biomass gasification-based power generation system consists of solid oxide fuel cell, supercritical carbon dioxide cycle and indirectly heated air turbine. *Clean Technol Environ Policy*. 2019;21(4):827-845.

18. Qiao Z, Tang Y, Zhang L, et al. Performance analysis and optimization design of an axial-flow vane separator for supercritical CO$_2$ (sCO$_2$)-water mixtures from geothermal reservoirs. *Int J Energy Res*. 2019;43(6):2327-2342.

19. Sharma OP, Kaushik SC, Manjunath K. Thermodynamic analysis and optimization of a supercritical CO$_2$ regenerative recompression Brayton cycle coupled with a marine gas turbine for shipboard waste heat recovery. *Therm Sci Eng Prog*. 2017;3:62-74.

20. Holaind N, Bianchi G, De Miol M, et al. Design of radial turbo-machinery for supercritical $CO_2$ systems using theoretical and numerical CFD methodologies. *Energy Procedia*. 2017;123: 313-320.

21. Lv G, Yang J, Shao W, Wang X. Aerodynamic design optimization of radial-inflow turbine in supercritical $CO_2$ cycles using a one-dimensional model. *J Energy Convers Manag*. 2018;165: 827-839.

22. Fleming DD, Conboy T, Pasch JJ, Rochau GA, Fuller RL, Holschul TV, Wright SA. Scaling consideration for a multi-megawatt class supercritical $CO_2$ Brayton Cycle and commercialization. 2013, Sandia National Laboratories Report SAND2013-9106.

23. Kalra C, Hofer D, Sevincer E, Moore J, Brun K. Development of High Efficiency Hot Gas Turbo-Expander for Optimized CSP Supercritical $CO_2$ Power Block Operation. paper presented at: 2014, 4th International Symposium – Supercritical $CO_2$ Power Cycles, September 9–10, 2014, Pittsburgh, USA.

24. McDowell M, Eastland A, Huang M, Swingler C. *Advanced Turbomachinery for sCO$_2$ Power Cycles*. Atlanta, GA: NETL University Turbine Systems Research Group; 2015.

25. Walton J, Heshmat H, Cordova JL. Technology Readiness of 5th and 6th Generation Compliant Foil Bearing for 10 MWe s-$CO_2$ Turbomachinery Systems. Paper presented at: Proceeding of the 6th International Supercritical $CO_2$ Power Cycle Symposium, March 27–29, 2018, Pittsburgh, Pennsylvania, USA.

26. Baker Hughes, Lujkin and Allen Gears Power Transmissions & Gearboxes. Retrieved on 02 September 2019 from https://www.bhge.com/midstream/lng/gearboxes

27. Giovannelli A, Archilei EM, Salvini C, Bashir MA, Messina G, Design of the Power Group for a 15 MW Supercritical Carbon Dioxide Plant. Paper presented at: 2019 4th International Conference on Smart and Sustainable Technologies, SpliTech 2019, https://doi.org/10.23919/SpliTech.2019.8783106

28. Messina G., sCO$_2$ Recompressed Cycle optimization, 2015, Internal Report.

29. Giovannelli A. Development of turbomachines for renewable energy systems and energy-saving applications. *Energy Procedia*. 2018;153:10-15.

30. Baljè OE. A study on design criteria and matching of turbomachines: Part A-Similarity relations and design criteria of turbines. *J Eng Power*. 1962;84(1):83-102.

31. Baljè OE. A study on design criteria and matching of turbomachines: Part B-Compressor and pump performance and matching of turbocomponents. *J Eng Power*. 1962;84(1): 103-114.

32. Lemmon EW, Bell IH, Huber ML, McLinden MO. NIST Standard Reference Database 23: Reference Fluid Thermodynamic and Transport Properties-REFPROP, Version 9, National Institute of Standards and Technology, Standard Reference Data Program, Gaithersburg, 2017

33. Stodola A. *Steam and Gas Turbines*. New York, NY: McGraw-Hill; 1927.

34. Aungier RH. Preliminary aerodynamic design of radial-inflow turbine stages. *Turbine Aerodynamics: Axial-flow and Radial-inflow Turbine Design and Analysis*. New York, NY: ASME Press; 2006:394.

35. Dixon SL, Hall CA. *Radial Flow Gas Turbines. Fluid Mechanics and Thermodynamics of Turbomachinery*. 6th ed. Burlington, VT: Butterworth-Heinemann; 2010.

36. Agromayor R, Nord LO. Preliminary design and optimization of axial turbines accounting for diffuser performance. *Int J Turbomach Propuls Power*. 2019;4(3):ijtpp4030032.

37. Daily JW, Nece RE. Chamber dimension effects on induced flow and frictional resistence of enclosed rotating disks. *J Basic Eng*. 1960;82:217-232.

38. Aungier RH. Mean streamline aerodynamic performance analysis of centrifugal compressors. *J Turbomach*. 1995;117:360-366.

39. Jansen W. A method for calculating the flow in a centrifugal impeller when entropy gradients are present. *Royal Society Conference on Internal Aerodynamics (Turbomachinery)*. London, UK: IME; 1967:133-146.

40. Johnston JP, Dean RC Jr. Losses in vaneless diffusers of centrifugal compressors and pumps. Analysis, experiment, and design. *J Eng Power*. 1966;88:49-62.

41. Rohlik, H.E. Analytical determination of radial inflow turbine design geometry for maximum efficiency; Technical note TN D-4384; NASA: Washington, DC, 1968, Retrieved on 10 January 2020 from https://ntrs.nasa.gov/search.jsp?R=19680006474

42. Japikse D, Baines NC. *Introduction to Turbomachinery, Concept ETI*. 1st ed. Oxford, England: Oxford University Press; 1999.

43. Liu X, Xuesong L, Jian S, Xiaodong R, Chunwei G. Design and analysis of S-$CO_2$ cycle and radial turbine for SOFC vehicle waste-heat recovery. *J Therm Sci*. 2019;28:559-570.

44. Pecnik R, Rinaldi E, Colonna P. Computational fluid dynamics of a radial compressor operating with supercritical $CO_2$. *J Eng Gas Turb Power*. 2012;134(12):122301.

45. Gibson, L., Galloway, L., Kim, S. Assessment of turbulence model predictions for a centrifugal compressor simulation. Paper presented at: Proceedings of the 1st Global Power and Propulsion Forum: GPPF 2017.

46. Aungier RH. A fast, accurate gas equation of state for fluid dynamic analysis applications. *J Fluids Eng*. 1995;117:277-281.

47. Blesgen T. Generalization of the Navier-stokes equations to two-phase flows. *J Phys*. 1999;32(10):1119-1123.

48. Allison TC, Smith NR, Pelton R, Jung S, Wilkes JC. Experimental validation of a wide-range centrifugal compressor stage for supercritical $CO_2$ power cycles. *J Eng Gas Turbines Power*. 2019;141(6):061011.

49. Ameli A, Afzalifar A, Turunen-Saaresti T, Backman J. Centrifugal compressor design for near-critical point applications. *J Eng Gas Turbines Power*. 2019;141(3):031016.

50. Ameli A, Afzalifar A, Turunen-Saaresti T, Gronman A, Backman J., Compressor design method in the supercritical $CO_2$ applications. Paper presented at: Proceedings of the 6th International Supercritical $CO_2$ Power Cycle Symposium, March 27–29, 2018, Pittsburgh, Pennsylvania, USA.

51. Ludtke KH. Process Centrifugal Compressors. *Compressor Design Constraints*. Berlin, Germany: Springer-Verlag; 2010. Chap. 4.

# APPENDIX A

**TABLE A1**  Final mesh details

| | Power-group (b) components | | | | | | Power-group (c) components | | | | | | | |
|---|---|---|---|---|---|---|---|---|---|---|---|---|---|---|
| | MC1 | MC2 | RC first stage | RC second stage | EXP1 | EXP2 | MC1 | MC2 | MC3 | RC first stage | RC second stage | EXP1 | EXP2 first stage | EXP2 second stage |
| Nodes (×10³) | 263.6 | 263.7 | 204.7 (rot.) 114.4 (stat.) | 503.9 | 396 | 396.9 | 263.3 | 261.1 | 265.7 | 204.7 (rot.) 114.4 (stat.) | 503.9 | 472.9 | 454,6 | 456.2 |
| Min. face angle | 22.4 | 27.1 | 20.2 | 22.2 | 17.7 | 26.4 | 25.6 | 33.1 | 30.3 | 20.2 | 22.2 | 31.1 | 29.5 | 35.2 |
| Max. face angle | 157.6 | 152.9 | 159.7 | 163.5 | 167 | 155.7 | 154.4 | 146.9 | 149.7 | 159.7 | 163.5 | 170 | 178.5 | 170.4 |
| Max. element volume ratio | 5.2 | 4.7 | 5.3 | 4.1 | 4.1 | 5 | 3.8 | 4.5 | 4.8 | 5.3 | 4.1 | 4.7 | 5.4 | 4.5 |
| Max. edge length ratio | 110.8 | 91.8 | 137.6 | 122.6 | 242 | 812 | 108.7 | 72.1 | 81.8 | 137.6 | 122.6 | 207.3 | 338.7 | 201.6 |

# APPENDIX B

## Recompressor (RC)

**TABLE B1**  RC preliminary design parameters

| | Preliminary geometry | |
|---|---|---|
| | **First stage** | **Second stage** |
| $\varphi_{1e}$ | 0.3 | 0.32 |
| $\chi_1$ | 0.6 | 0.72 |
| $b_2/D_2$ | 0.045 | 0.031 |
| $\varphi_2$ | 0.26 | 0.26 |
| $\psi_2$ | 0.68 | 0.7 |
| $\chi_2$ | 1.9 | 1.9 |
| $n_S$ | 0.51 | 0.42 |
| $D_S$ | 4.9 | 5.9 |

**TABLE B2** Results for preliminary and final RC design

| | First stage | | Second stage | |
| --- | --- | --- | --- | --- |
| | Preliminary geometry | Final geometry | Preliminary geometry | Final geometry |
| Impeller | | | | |
| $Z_g$ | 14 | 10 | 14 | 10 |
| $\beta_{2c}$ (°) | 55° | 34° | 58° | 26° |
| $D_{in}$ (mm) | 104 | 114 | 104 | 122 |
| $h_{in}$ (mm) | 26 | 29 | 17 | 12 |
| $D_{out}$ (mm) | 202 | 200 | 198 | 200 |
| $h_{out}$ (mm) | 9 | 8 | 6 | 5 |
| Vaned diffuser | | | | |
| $Z_s$ | 19 | 19 | 19 | - |
| $D_{out}$ (mm) | 300 | 300 | 383 | 383 |

# Main Compressor (MC)

**TABLE B3** MC preliminary design parameters

| | Preliminary geometry | |
| --- | --- | --- |
| | First stage | Second stage |
| $\varphi_{1e}$ | 0.53 | 0.44 |
| $\chi_1$ | 0.39 | 0.55 |
| $b_2/D_2$ | 0.08 | 0.06 |
| $\varphi_2$ | 0.33 | 0.32 |
| $\psi_2$ | 0.63 | 0.68 |
| $\chi_2$ | 2.1 | 1.8 |

**TABLE B4** Results for preliminary and final MC design

| | First stage | | Second stage | |
| --- | --- | --- | --- | --- |
| | Preliminary geometry | Final geometry | Preliminary geometry | Final geometry |
| Impeller | | | | |
| $Z_g$ | 15 | 15 | 15 | 15 |
| $\beta_{2c}$ (°) | 42° | 64° | 45° | 48° |
| $D_{in}$ (mm) | 116 | 116 | 111 | 111 |
| $h_{in}$ (mm) | 25.5 | 25 | 32 | 32 |
| $D_{out}$ (mm)] | 244 | 244 | 200 | 200 |
| $h_{out}$ (mm) | 20 | 25 | 12 | 11 |
| Vaned diffuser | No | No | No | No |

**TABLE B5** Configuration 2c MC: preliminary design parameters

| | First stage | Second stage | Third stage |
| --- | --- | --- | --- |
| $\varphi_{1e}$ | 0.67 | 0.67 | 0.67 |
| $\chi_1$ | 0.51 | 0.77 | 0.87 |
| $b_2/D_2$ | 0.034 | 0.019 | 0.012 |
| $\varphi_2$ | 0.31 | 0.27 | 0.24 |
| $\psi_2$ | 0.73 | 0.75 | 0.75 |
| $\chi_2$ | 2.77 | 2.25 | 2.13 |

**TABLE B6** Configuration 2c Results for preliminary and final MC design

|  | First stage | Second stage | Third stage |
|---|---|---|---|
| Impeller |  |  |  |
| $Z_g$ | 15 | 15 | 15 |
| $\beta_{2c}$ (°) | 17 | 17 | 22 |
| $D_{in}$ (mm) | 148 | 212 | 245 |
| $h_{in}$ (mm) | 48 | 27 | 17 |
| $D_{out}$ (mm)] | 410 | 478 | 522 |
| $h_{out}$ (mm) | 14 | 9 | 6.5 |
| Vaned diffuser | Yes | Yes | Yes |

## Expanders

**TABLE B7** Results for preliminary and final EXP1 and EXP2 design (configuration 2b)

|  | EXP1 | | EXP2 | |
|---|---|---|---|---|
|  | Preliminary geometry | Final geometry | Preliminary geometry | Final geometry |
| Impeller |  |  |  |  |
| $Z_g$ | 7 | 7 | 7 | 7 |
| $\beta 1c$ (°) | 22 | 30 | 90 | 90 |
| $D_{in}$ (mm) | 300 | 300 | 450 | 450 |
| $h_{in}$ (mm) | 30 | 17 | 19 | 18 |
| $D_{out}$ (mm) | 160 | 150 | 240 | 240 |
| $h_{out}$ (mm) | 70 | 50 | 39 | 39 |

**TABLE B8** Results for preliminary and final EXP1 and EXP2 design (configuration 2c)

|  | EXP1 | | EXP2 first stage | | EXP2 second stage | |
|---|---|---|---|---|---|---|
|  | Preliminary geometry | Final geometry | Preliminary geometry | Final geometry | Preliminary geometry | Final geometry |
| Impeller |  |  |  |  |  |  |
| $Z_g$ | 7 | 7 | 14 | 14 | 14 | 14 |
| $Z_n$ | - | - | 13 | 13 | 13 | 13 |
| $\beta 1c$ (°) | 40 | 40 | 90 | 90 | 90 | 90 |
| $D_{in}$ (mm) | 195 | 195 | 690 | 690 | 690 | 690 |
| $h_{in}$ (mm) | 20 | 20 | 15 | 15 | 22 | 22 |
| $D_{out}$ (mm) | 107 | 107 | 324 | 324 | 324 | 324 |
| $h_{out}$ (mm) | 50 | 50 | 55 | 55 | 55 | 56 |